POLITECNICO DI TORINO

Master's Degree in Biomedical Engineering

Imperial College London

Master's Degree Thesis

Instrumented finger platform for a systematic investigation on the control of hand exoskeletons with compliant materials

Supervisors

Prof.ssa Gabriella OLMO

Prof. Dario FARINA

Hsien-Yung HUANG

Candidate

Mattia BISIO

July 2020

Abstract

A high number of traumas and neurophysiological disorders each year, along with the aging population, has increased the number of people with compromised hand functionality. The need of providing rehabilitative and assistive devices for patients has encouraged the study in hand exoskeletons. Since rigid structures are bulky and may cause fatigue, soft and compliant components have gained attention from the researchers, as they can provide better wearability, improve the portability and help in performing more natural movements.

The aim of the project is to develop an instrumented testing platform to allow a systematic investigation into the control of a hand exoskeleton made with compliant materials. The platform is comprised of a 3D-printed finger with angular position sensors, a load cell to measure the endpoint force and a DC motor which controls the exoskeleton through a cable-driven system. The device allows to perturb the finger with a cyclic motion, both in the air and touching the load cell. Furthermore, a Lagrangian model was proposed to map the motor torque to the fingertip force.

In order to validate the testing platform, two stages of identification process have been performed to evaluate the missing parameters of the model and then to predict the fingertip force. The first phase of the experiment provides for a repeated sine wave disturbance which moves the finger in the air by means of a single extension wire. Using the acquired data, a simple linear regression is used to estimate the missing parameters of the Lagrangian model: tension moment arm and friction loss. The algorithm is applied by dividing the joints motion in four different regions.

During the second phase, the instrumented finger is placed in contact with a compression load cell and a cyclic motion is applied to the flexion cable to allow finger flexion. Implementing the estimated parameters acquired in the first phase, it is possible to evaluate the exerted endpoint force by knowing the cable tension, which is indirectly measured from the motor torque.

The preliminary results indicated that our approach to simplify the dynamic equations with the Lagrangian model was not satisfying, with low accuracy in terms of shape ($R^2 = 0.36 \pm 0.13$) and large prediction jumps which are due to state transition. Moreover, a time delay between predicted and measured force has been detected.

To further improve the model, parameters estimation has been updated and simplified by using one single couple of parameters for the entire acquisition. To evaluate the time delay, two alternative solutions based on a similarity measure have been proposed. The most promising technique, which minimises the squared Euclidean distance, compensates the delay and allows to have a good fit in terms

of shape ($R^2 = 0.97 \pm 0.01$). However, the peak amplitude of the model is around four times lower than the measured one.

Considering the complexity of the research field, the limited time available allowed to face the first issues of the system, but it has not been possible to further improve the research and incorporate the actual model for developing an open-loop controller. However, as results are highly reproducible, a better force prediction can be achieved by upgrading the platform with a pretension mechanism for the exoskeleton cable and by improving the parameters estimation.

Table of Contents

List of Tables

List of Figures

Acronyms

ABS
Acrylonitrile Butadiene Styrene

ADL
Activities of Daily Living

BOM
Bill Of Materials

CAD
Computer Aided Design

CMC
Carpometacarpal

DIP
Distal Interphalangeal

DOF
Degree Of Freedom

FFF
Fused Filament Fabrication

GUI
Graphical User Interface

LHS
Left Hand Side

MCP

Metacarpophalangeal

PLA

PolyLactic Acid

PIP

Proximal Interphalangeal

PWM

Pulse Width Modulation

QOL

Quality Of Life

ROM

Range Of Motion

STL

STereoLithography

SCI

Spinal Cord Injury

Chapter 1

Introduction

As hand exoskeleton research is focusing on the use of new soft materials, such as silicone and polyurethane rubbers, it is becoming of great importance to understand how the motor torque applied is translated into output force and how the combination of exo-component design and cable routing have an impact on this outcome. In addition, getting familiar with this subject would open new horizons in the development of a real-time controller.

The aim of this project is to develop an instrumented platform to systematically test different cable-driven exoskeleton designs and consequently to propose a relation between the motor torque and the exerted endpoint force by using a dynamic Lagrangian model.

For this purpose, a specific testing platform equipped with a 3D-printed finger is developed. Within the finger structure, angular sensors are installed to measure joint positions. While the motor perturbs the finger through repeated motions, the system acquires joints' angular position and motor torque. The acquired data, in combination with a linear regression method, allow to estimate the moment arm and the friction loss of a dynamic model based on Lagrangian approach. Once model parameters are known, the finger is repeatedly moved towards a load cell to measure the endpoint force and data are once again acquired. The last step consists in using the proposed model to predict the endpoint force and to evaluate the estimation accuracy compared to the measured force.

The thesis is organised in six chapters: the next sections of Chapter 1 give a concise description of hand skeletal and muscular districts and an overview on rigid

and soft exoskeleton devices. Chapter 2 highlights the main characteristics of the instrumented platform and selected sensors, while Chapter 3 explains in detail the experiment protocol and how the Lagrangian model is derived. Chapter 4 presents experimental data, focusing on parameters estimation and force prediction. Finally, Chapter 5 and 6 discuss achieved results and their limits, suggesting alternative solutions for future works.

1.1 Anatomy of the hand

The development of a hand exoskeleton is a complex process that firstly requires an adequate knowledge of the hand anatomy, in order to make appropriate choices during the design stage and to provide a safe assistive device. From this point of view, it is a good practice to respect the physiological range of motion (ROM) of each joint and consequently to avoid dangerous unnatural motions. Moreover, hand is one of the most intricate body part, as a lot of muscles and a high number of degrees of freedom (DOFs) are involved to control the movement. It is clear that this characteristic makes the study of effective solutions even more complicated.

Beginning from the skeletal frame, hand bones are grouped in two main structures, namely carpus and metacarpus: the first one is composed by eight bones and is directly articulated with radius and ulna through the wrist joint, whereas the second one is made of five bones, connected to the carpus on the proximal end and to the proximal phalanx of each finger on the distal end, as shown in Figure 1.1. The joints which connect carpal bones to metacarpal units are generally called carpometacarpal (CMC) joints, but they show many differences. For example, the thumb exhibits a sellar joint (a concave and a convex surfaces that oppose each other) that allows two different degrees of freedom, abduction/adduction and flexion/extension. Index, middle and ring CMC joints are plane and with only one DOF, whereas the little finger joint is a semi-saddle one with conjunctional rotation [1].

Metacarpophalangeal (MCP) joints link the metacarpal unit of each finger to the proximal phalanx and they are defined as condylar joints, the same type present in wrist and knee joints: they provide two DOFs. Shifting towards the tip of the fingers are the proximal interphalangeal (PIP) and distal interphalangeal

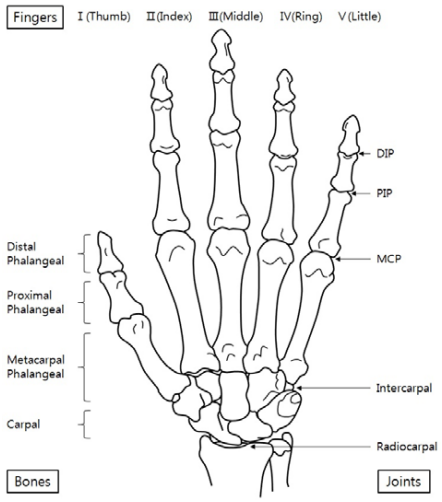

Figure 1.1: Bones and joints of the human hand (dorsal view). Adapted from [1].

(DIP) joints. They are both bicondylar with one DOF, that is flexion/extension. Concerning interphalangeal joints, it is interesting to point out that, although they are considered to have one fixed axis of rotation, they actually change with respect to the degree of motion in flexion and extension.

Different postures and configurations that a human hand can achieve are managed through articulated muscular regions: they can be divided in two main subgroups, that are composed by intrinsic and extrinsic muscles. The first group is made up by muscles placed deep within the hand which are responsible for independent and subtle motion of each finger. Lumbrical, dorsal and palmar interossei belong to this family. The second group is constituted by muscles originating from the forearm and placed closer to the skin, mainly long finger flexors and extensors. In addition, this category controls the closure of the whole hand and the wrist flexion.

Another important role in hand motion is managed by tendons and ligaments. When a finger changes its position, both flexor and extensor tendons modify their excursion to allow natural movements. With regard to this behaviour, some studies also proved that linear and non-linear relationships can be found between the amount of tendon excursion and angle displacements in MCP, PIP and DIP joints [2]. Each finger has five annular and three cruciate ligaments placed on the palmar side and made by the fibrous layer of the tendon sheaths. These components

basically work as pulleys through which the flexor tendon slides, maintaining the position along the longitudinal axis and then avoiding the bowstring phenomenon. The functionality of tendons in hand motion has drawn attention of researchers and led to several bio-inspired hand exoskeleton developments [3].

The combined attribution of all aforementioned elements is reflected in the defined range of motion for each finger joint. In literature, several studies and medical books have tried to analyse the joints' ROM under different conditions. According to Hirt et al. [4], the ROM of MCP joints (excluding the thumb, which has a specific structure, different from the other four fingers) is between 90° in flexion and 40° in extension. PIP joints typically have a greater maximum angle of flexion, as they can reach up to 130°, but they are almost unable to hyperextend beyond zero position. DIP joints can flex up to 90° and extend up to 30°. However, in these joints extension deeply depends on the laxity of the ligaments and for this reason the maximum angle has a great variability across the population.

Bain and al. [5] carried out a study on the functional ROM based on the Sollerman test, which is a standardised hand function test that demands to grasp twenty common objects used in daily living. Results obtained are shown in Table 1.1. Looking at the data, mean active ROM is slightly lower than values presented in [4], as in this case they are achieved doing a precise set of grasps. Moreover, mean functional ROM is on the right-hand side of Table 1.1, where it is defined as the range of motion required to complete 90% of all tasks.

These listed values, derived from two different sources, provide an idea of

Table 1.1: Mean active and functional range of motion based on ten healthy subjects performing Sollerman test. Data are expressed in degrees. Adapted from [5].

	Active ROM		**Functional ROM**	
	Extension	Flexion	Extension	Flexion
MCP	-19 (SD 6.9)	90 (SD 9.1)	19 (SD 12.2)	71 (SD 8.1)
PIP	-7 (SD 3.7)	101 (SD 8.3)	23 (SD 8.7)	87 (SD 6.5)
DIP	-6 (SD 4.1)	84 (SD 8.5)	10 (SD 7.9)	64 (SD 8.1)

the typical finger joints' ROM and constitute a good starting point to approach exoskeleton development.

1.2 State of the art

Hand functionality can be compromised by a large number of injures, traumas and neurological disorders, among which spinal cord injury (SCI), traumatic brain injury (TBI) and stroke are the most common and constantly increasing in the last years. In fact, according to [6], more than 665,000 people survive a stroke each year in the US and after six months 50% of them still have a certain degree of hemiparesis. In Europe, recent analysis [7] have revealed that age-adjusted incidence stroke rate, as well as mortality stroke rate, are decreasing, but the overall number of stroke cases per year is increasing due to population ageing. That is why governments and healthcare systems will have to deal with a higher number of people who will suffer post-stroke consequences and to assure them long-term medical care and rehabilitation.

It is important to highlight that partial or complete loss of the hand function has a great impact on the patient's quality of life (QOL), reducing the ability to perform even simple tasks autonomously, such as using a key, getting dressed or grabbing a cup. Therefore, researches have been focused on the development of assistive and rehabilitative wearable devices, with the aim of providing continuous at-home assistance and improving functionality recovery through robotic repetitive motions.

Technologies used in this field are constantly evolving, as evidenced by various reviews on dynamic hand orthoses and exoskeletons. In 2016 Bos et al. [8] presented an organized overview of 165 devices, where each mechatronic component is classified according to a framework with signal, energy and mechanical domains. According to their study, it is interesting to point out that there has been a clear growth in the development of these devices in the five-year period 2011-2015. Moreover, greater attention has turned towards home rehabilitation and daily assistive tools, consolidating the trend of developed countries to bring medical care directly at home.

Main features reported in [8] can be described as following: in the actuation

branch, the most common solution is represented by electromagnetic components (i.e. DC motors), followed by pneumatic systems. The former are cheaper and require less maintenance, but the use of gears and planetary heads makes efficiency lower. The latter have easier power transmission methods, yet they are less durable and can have many undesirable issues. In the mechanical field, the number of feasible choices has to be divided into transmission methods, where pulley-cable and Bowden cable systems are the main popular when motors are the chosen actuators, and mechanism, further classified in structure, joint articulation, underactuation and constraints. Looking at the data distribution in these last categories, it is evident the increasing number of portable devices and the use of monocentric joint solutions, even though a quite large amount of polycentric and jointless systems are still developed.

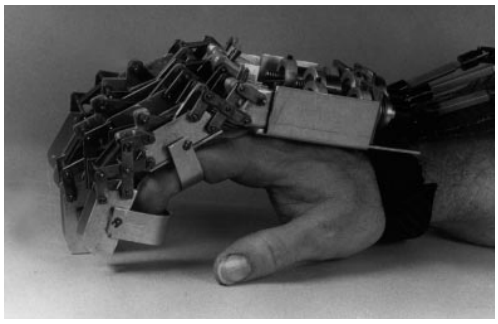

(a) Shields' exoskeleton. Adapted from [9].

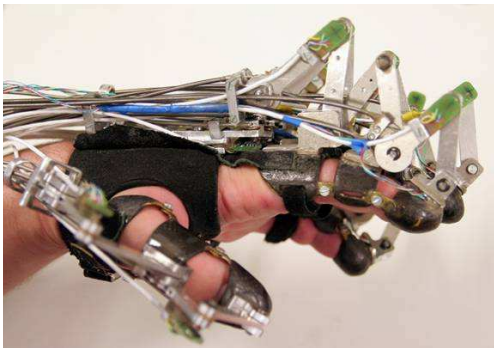

(b) Wege's exoskeleton. Adapted from [10].

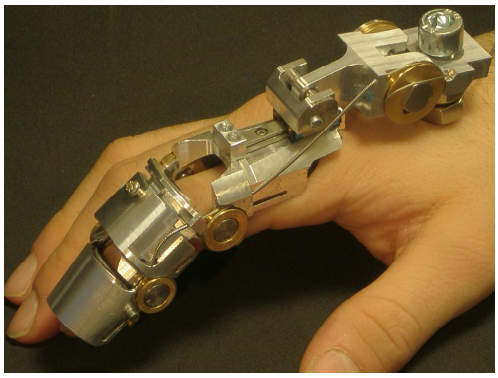

(c) HANDEXOS. Adapted from [11].

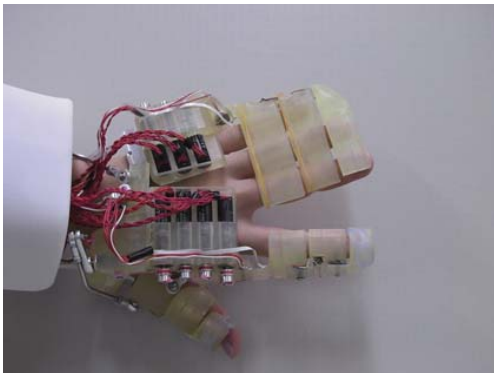

(d) Hasegawa's exoskeleton. Adapted from [12].

Figure 1.2: Examples of rigid hand exoskeletons from different research groups.

Inspired by lower and upper limb technologies, several research teams began to

propose rigid exoskeleton-type devices to perform rehabilitation protocols, to reduce therapists' workload and to assess performance quantitatively [9], [10], [11], [12]. However, this kind of solutions (Figure 1.2) are mainly limited to the clinical environment, due to their bulky structure, high costs and low portability. Also, the possible misalignment between robot axes and human fingers is a drawback which should be taken into account. Moreover, it is important to remind that rehabilitation by itself does not ensure a complete restoration of hand functions and a lot of patients still need help from robot assistive devices to carry out activities of daily living (ADL) properly. As a consequence, research attentions are moving towards soft wearable robotic hands, in order to obtain compliant and fully portable devices that can be worn for a long time without affecting the natural movement of other joints.

Shahid et al. [13] presented a summary of various soft hand exoskeletons between 2008 and 2018, concentrating mainly on technological tendencies and how the way to design these devices has changed from rigid materials. The challenge lies in making light and compact wearable gloves while ensuring the correct amount of force to the fingers. The first distinction is between pneumatic and electric actuator mechanisms: despite pneumatic systems allow to use easier control strategies, as pressure is uniformly applied to the finger and kinematics can be measured with no apparent effort, compressors greatly increase the weight of the whole device, affecting their portability. Nevertheless, the paper shows that the number of publications concerning pneumatic actuators increased in the last years. On the other hand, tendon-pulley mechanisms just have to maintain a certain cable tension to supply the requested output force and for this reason they still represent a large segment in the soft exoskeleton research field.

One of the first example of soft glove is SEM, proposed by Nilsson et al. [14] in 2012 and intended to improve wearer's grasping capability. In detail, this device is a textile glove with integrated force sensors that actuates three fingers (thumb, middle and ring, in Figure 1.3a) using individual artificial tendons. The motion is controlled by a separate power unit worn on the shoulders as a backpack, thus avoiding additional weight on the hand.

A different way to approach finger actuation can be found in SNU Exo-Glove presented by In et al. [16, 15]. Their jointless structure avoids issues of conventional

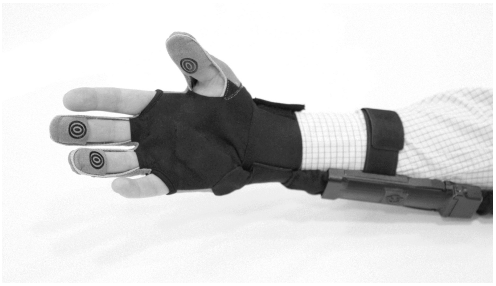

(a) SEM glove. Adapted from [14]

(b) SNU Exo-Glove. Adapted from [15]

Figure 1.3: SEM glove and SNU-Exo glove designs.

pin joint robots, such as frame interference and coaxial matching with centres of rotation, and allows to control all three joints with one single wire. They also introduced an innovative differential mechanism by which is possible to flex more than one finger at a time, using a single wire and a system of pulleys. In this way, fingers can adapt to the shape of the grasped object.

The first design has been improved [17] and it can be observed in Figure 1.3b, up to replace the fabric glove with silicone components [18]. The use of a polymer transforms the design and fabrication process. In fact, the silicone glove has different compliance and wearability with respect to a classic fabric glove and every detail has to be carefully designed, as it is not possible to add any additional component once the part is ready. Figure 1.4 shows the main characteristics of the Exo-Glove Poly: wires go through Teflon tubes embedded in thimbles and straps (placed along the finger) and then they reach the main body, which has some dedicated features to confer stretchability and actuation adjustments, such as the diamond shapes on the dorsal side. Furthermore, this innovative device allows the sanitization of each component just using alcoholic solutions and hence it is promising to be used several times by multiple users.

Design innovations and the search for more comfortable and efficient solutions have to be supported by kinematic and dynamic analysis of the device. In this context, an interesting strategy is the one presented by Pu et al. [19, 20]. Their wearable hand exoskeleton for rehabilitation is designed to provide flexion/extension

Figure 1.4: Dorsal and palmar view of Exo-Glove Poly. Wires slide through silicone thimbles and straps, up to reach the main body in the palmar area. Adapted from [18]

motion for each joint of the finger using cable transmission. In order to study how cable tension varies when the finger assumes different positions, they proposed an exoskeleton's dynamic model based on Lagrangian approach and they validated it doing direct tension measurements.

Taking advantage of this method, it is possible to investigate the finger behaviour when using a soft exoskeleton and to search for a relation between motor torque and endpoint force. In fact, it is clear that the orientation towards soft materials requires a thorough knowledge of their mechanical properties, but a further analysis is needed to study how different exoskeleton designs influence the device output in terms of force. This point is crucial if the goal is to help patients, giving them better solutions that dispense the correct amount of assistance to perform ADL. For this reason, the development of an instrumented platform that can investigate different settings and cable routings is of major importance. Furthermore, the possibility to identify a relation between motor torque and exerted force could directly affect the way devices are programmed, by encouraging real-time control solutions using angular position and force feedback.

Chapter 2

Testing platform design

The investigation of the behaviour of a finger subjected to repeated motions requires the development of a specific testing platform. The goal is to implement a measuring system for cable-driven exoskeletons with an artificial finger unit. The developed system is intended to measure finger joints' angular displacement and the resulting endpoint force exerted by the artificial fingertip. The platform is also comprised of a DC motor which performs flexion and extension movements by running a cable-driven exoskeleton. The complex of motor and all the sensors is managed by a real-time controller and a target PC via LabVIEW ® environment.

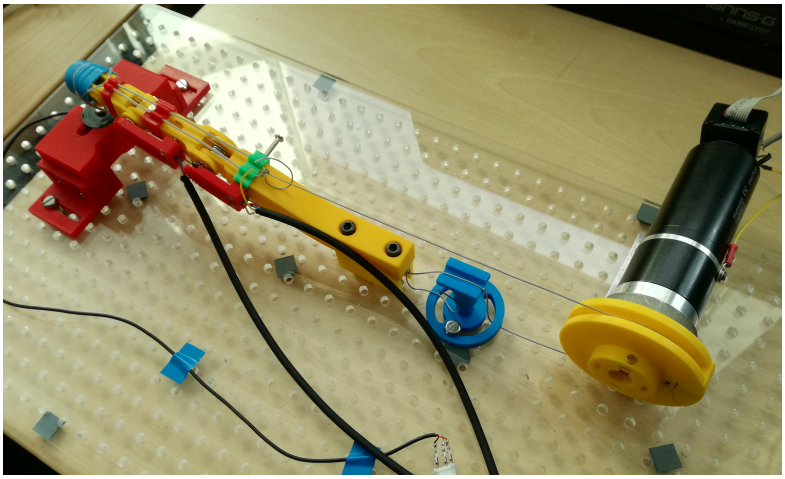

Figure 2.1: Instrumented testing platform. The DC motor, placed on the right side of the platform, moves the cable to control the artificial finger. The load cell is positioned in correspondence of the fingertip unit.

Each component of the equipment, which is shown in Figure 2.1, is described into this chapter in detail, focusing on the design of the instrumented finger, sensors and motor-controller system architecture.

2.1 Instrumented finger

The instrumented finger aims to replicate the mechanical properties of a human finger and to be able to measure joints' displacements during controlled motions.

The idea was adapted from Rose et al. [21, 22], where the complete device has been designed to provide a low-cost and open-source instrumentation to validate joints' position and to evaluate torque effect in soft robotic gloves. In fact, even though there are many commercially available technologies to study hand motion, most of them cannot be easily equipped with position sensors. Moreover, despite the fact that motion capture systems are effective tools to investigate in hand kinematics, they are expensive and not time effective in terms of calibration and set up. Therefore, there is a clear need of an easy-to-use and cheap solution such as Rose's Instrumented Hand.

The system was originally presented as a three-fingered hand, with thumb, index and middle fingers. Most components are 3D printed, so as to reduce fabrication time and cost, and integrated with mechanical parts, including three torsion springs placed between phalanges to replicate finger joint stiffness during flexion and extension. The concept of approximating joints using rotary pins such as springs is endorsed by many studies, which have shown the possibility to simplify

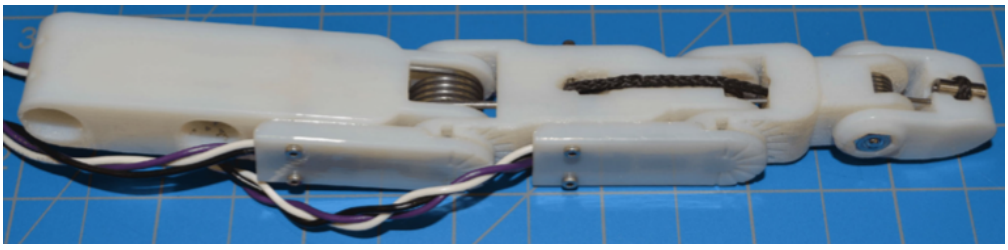

Figure 2.2: Finger of the Instrumented Hand proposed by Rose's research group. A black tendon made of fabric couples the motion of middle and distal phalanges, while three torsion springs allow flexion/extension movement for each joint. Adapted from [21]

the complicated movement of fingers' joints without losing in terms of accuracy. Figure 2.2 shows a single finger of the Instrumented Hand proposed by Rose: torsion springs are clearly visible between each phalanx, while a tendon-inspired cable that slides through the phalanges is used to couple PIP and DIP motion, in order to replicate what happens in a human hand. On the lateral side of MCP and PIP joints, angular position is measured by a magnetoresistive angular sensor, coupled with a circular neodymium magnet. As joint rotation is performed, the sensor placed over the magnet perceives a change in the magnetic field and this is reflected in a different voltage output that can be measured by an external data acquisition system.

All these characteristics are an excellent starting point to develop the instrumented finger needed for the project. However, some adjustments are required to make it suitable for the main purpose and compliant with respect to the perforated plastic base used to fix each part of the system. As clearly illustrated in Figure 2.2, Rose's finger is made up by four different units, which simulate the metacarpal bone and the three phalanges of a real finger. Looking at the metacarpal component, it can be observed that it has two holes that allow to fix the finger on the lateral side, thus avoiding the effect of gravity when placed on a horizontal plane. This feature is functional to secure the instrumented finger, but it does not account for alternative orientations.

In this project, the testing platform wants to mimic a hand leaning on a flat surface and to take into account the gravitational field. Therefore, holes have to be arranged on the other side of the metacarpal unit.

Furthermore, the first phase of the experiment needs a finger that is able to move in the air freely and to test its motion during both flexion and extension. Concerning this, the metacarpal unit from Rose's work is plane and it does not allow the index finger to move in both directions when fixed to a platform. Moreover, it does not simulate a natural position of the finger when the human wrist is positioned over a surface, as shown in Figure 2.3. Thus, it seemed reasonable to propose a metacarpal unit with a curvature of 15°, in order to reproduce the wrist extension angle.

Finally, finger's dimensions have to be changed, so as to be similar to the ones of my index finger. This choice is due to the fact that originally my finger was

Figure 2.3: Lateral view of a human hand. The position of the index finger is the one simulated building the instrumented testing platform.

intended to be used with the exoskeleton, in order to make comparisons after preliminary tests with the instrumented one.

Once necessary changes have been discussed, the original CAD files can be downloaded from Mahi (Mechatronics and Haptic Interfaces) Lab website [23] and modified accordingly, using Autodesk ® Fusion360 as mechanical design software. Figure 2.4 shows the updated version of the metacarpal unit, with two holes for M5 screws to fix it to the support platform and a 15° angle to mimic wrist extension.

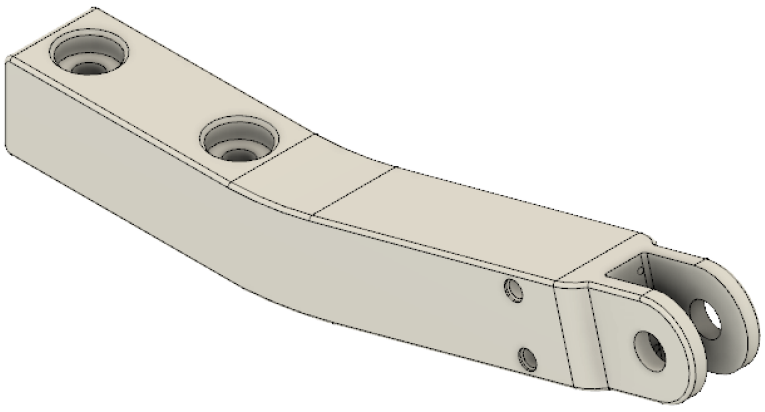

Figure 2.4: Metacarpal unit of the instrumented finger. Close to the holes used to fix the finger to the platform (left side), it is visible a curvature of 15° that simulates wrist extension when the hand leans on a flat surface.

On the lateral side are visible other two small holes that are intended for placing an angular sensor with its cover. On the right side, the space between the rounded ends of the metacarpal component is destined for the torsion spring.

With respect to the metacarpal unit, phalanges have been modified to a lesser extent, as it was decided to maintain their original shape. Nevertheless, each unit had to be customized according to the selected mechanical components. In fact, despite Mahi Lab website makes available a detailed bill of materials (BOM) to complete the finger, most of the components come from the American market and therefore it has been necessary to find equivalent or similar pieces purchasable in the European market, in order to save time and money in the development phase. One of the most critical research was for the ring magnet, since the angular measurement system requires a diametrical magnetization but the greatest amount of commercial magnets is axially magnetised. The lack of available solutions has compelled to use a magnet with a different size and then to rearrange its place on the lateral side of the finger.

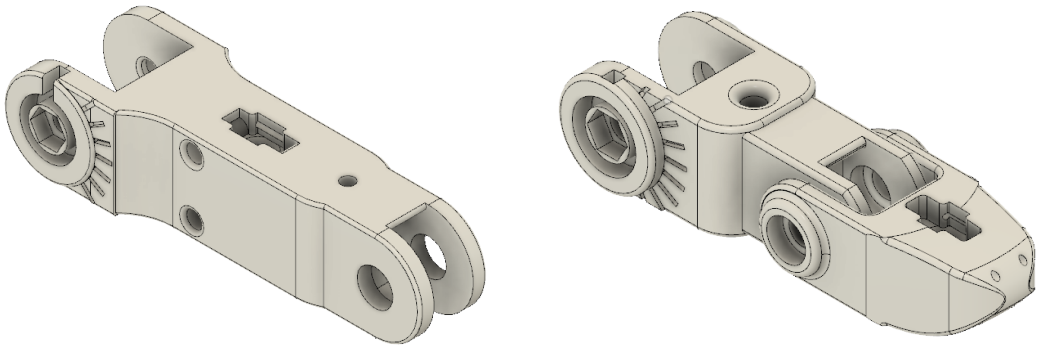

(a) Proximal phalanx **(b)** Middle and distal phalanges

Figure 2.5: Phalanges of the instrumented finger. Each phalanx, 3D printed using ABS, has been designed to be matched with mechanical components and torsion springs.

Figure 2.5 shows the final versions of the phalanges of the instrumented finger. On the left side of proximal and middle ones, there are allocated circular gaps for neodymium magnets.

When every detail is settled, finger units are 3D printed using acrylonitrile butadiene styrene, commonly known as ABS, which is one of the most common

plastic materials used in rapid prototyping, as well as PLA (polylactic acid). 3D printers used for this process are based on fused filament fabrication (FFF) technology (Figure 2.6): a filament of thermoplastic material is heated in the printer head and extruded on the printing platform to build up the object layer by layer. In fact, before the printing process begins, a dedicated software mathematically slices an STL file (STereoLithography format) of the component into different layers. The nozzle is moved in a horizontal plane to deposit the plastic material and once a layer is ready, the build plate is vertically moved in order to start the next one. The main advantage of this technique, compared to other 3D printing technologies

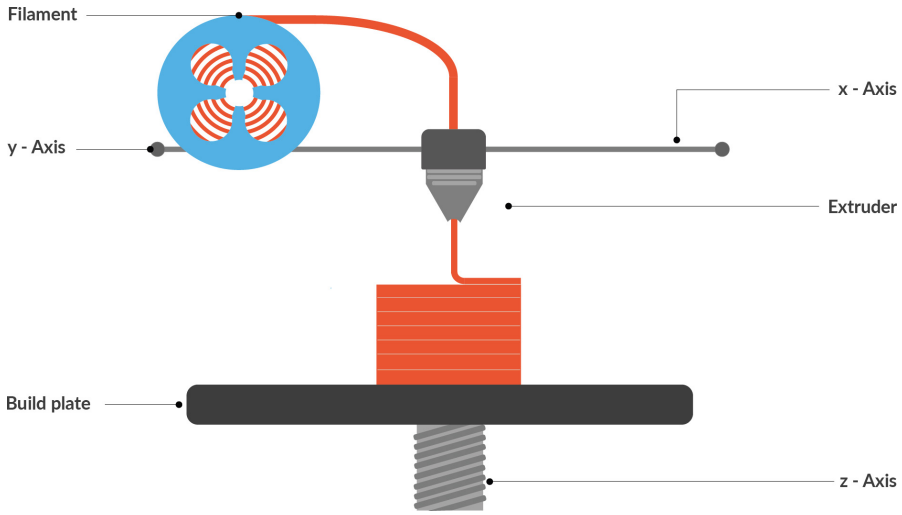

Figure 2.6: Fused filament fabrication technology. The plastic filament is heated and extruded to build the object layer by layer. When a layer is completed, the build plate moves down along the z-axis. Adapted from [24]

such as photopolymerisation, is a lower cost of materials, that gives more freedom to the user in making several attempts during the design phase. However, in terms of resolution and precision, other technologies are preferable.

Once 3D-printed units are ready, torsion springs are assembled. Their role in the instrumented finger is extremely important, as they simulate joint stiffness and allow to provide one DOF (flexion/extension) in each joint. This category of springs store mechanical energy when twisted and exert a torque in the opposite direction, that is proportional to the bending angle. For this project, three different torsion springs have been selected: the biggest one is intended to mimic the MCP

joint and can exert the highest torque, while the smallest one is for DIP joint. They are all made of stainless steel and their zero position corresponds to a straight angle. Each phalanx has specific holes to insert spring legs: when the mandrel is correctly positioned and aligned to the joint, the spring is blocked using an M3 screw with its respective nut. In this way, two adjacent phalanges can properly simulate the flexion/extension movement, without experiencing any misalignment during the motion.

Afterwards, each additional component has to be fixed by means of screws and nuts. On the lateral side of MCP and PIP joints, neodymium magnets are pushed into their gaps and angular sensors are fixed above them using 3D-printed covers. On the contrary, DIP joint was not intended to be studied during exoskeleton motion and therefore it does not have any angular sensor on its side. When the finger is finished, it can be attached to a perforated platform made of rigid plastic. Its holes, distributed over several rows and columns, are arranged to fix all the other components needed for the system, in particular the load cell and the motor.

2.2 Load cell and angular sensors

Within the system, the load cell is meant to measure the endpoint force exerted by the finger during exoskeleton control. In literature, finger force during common daily activities is in the order of a few units or at most tens of Newton for each finger and existing soft devices show a similar force output. Therefore, in the context of an extended market of compression load cells, the research was focused on a cost-effective, small range and accurate sensor.

After a brief analysis, the choice fell on FC2231 developed by TE Connectivity, with 0-10 lbf range (0-44.5 N): its characteristic are shown in Table 2.1. First of all, this linear angular sensor is compact, highly reliable and with very low deflection. Moreover, the selected version is already amplified and it does not need any additional circuitry to read output values.

In order to have the possibility to change the load cell height depending on the chosen experiment, an adjustable load cell container has been designed with the same CAD program as for the finger and 3D printed using FFF technology. In particular, the container is made up of three different components: two L-shaped

Table 2.1: Main characteristics of FC2231 compression load cell by TE Connectivity.

Parameters	**Min**	**Typ**	**Max**	**Unit**
Span	3.8	4	4.2	V
Zero force output	0.45	0.5	0.55	V
Accuracy		±1		% span
Temperature error - Zero	-1.25		1.25	% span
Temperature error - Span	-1.25		1.25	% span
Excitation voltage	4.75	5	5.25	V_{DC}

supports and one element that actually hold the load cell. The way the L-shaped pieces are designed allows to change the sensor positioning, moving it closer or farther away from the finger endpoint and then allowing more limited or extended ROM in flexion. Figure 2.7 shows the container in two different positions: to adjust the height, the container has to be unlocked and then locked again using two screws for each support. The holder has to be positioned between the vertical walls of the support units.

Before starting any kind of experiment, the load cell has been calibrated by

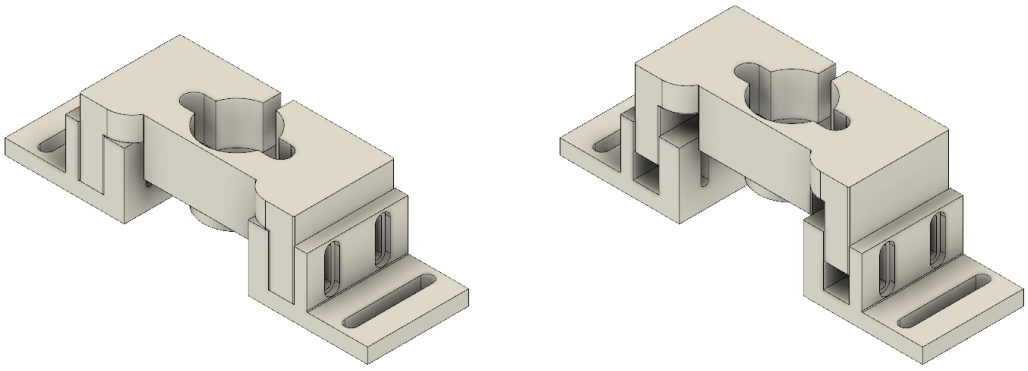

(a) Lower position **(b)** Higher position

Figure 2.7: Load cell container. The horizontal hole of the support, visible on the right side of each figure, is used to fix the container to the platform, while two vertical holes are used to fix the container to each support and to change its height.

adding several weights one at a time. The voltage output has been measured using a NI PCIe-6343 DAQ and a NI 68-pin connector block, which are already integrated in the system that will be used for motor control and data acquisition. The recording, with a sampling frequency of 20 Hz, begins with fifteen seconds

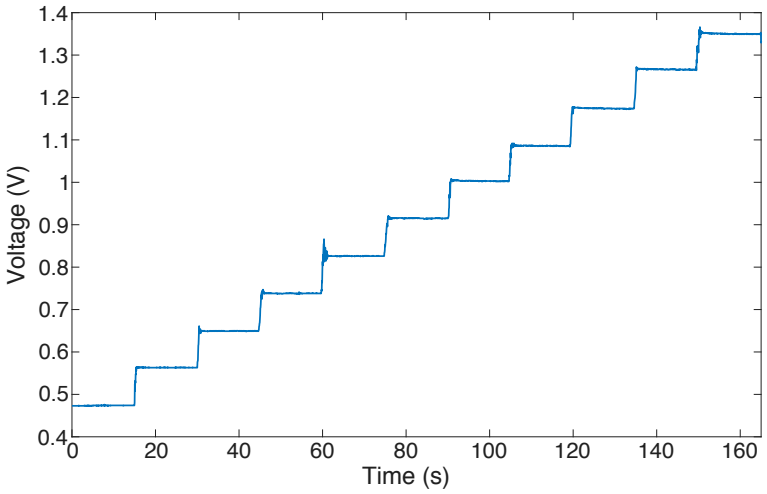

Figure 2.8: Voltage data used for load cell calibration. Every fifteen seconds, a weight of 100 grams is placed over the load cell, up to reach one kilogram.

without additional loads. After this period, a single weight is manually placed over the load cell and other fifteen seconds elapse before placing another weight. The operation is repeated until a load of one kilogram is reached. Once the acquisition is over, the voltage data shown in Figure 2.8 are processed to obtain a linear relationship between voltage and force.

To avoid any disturbance occurred adding weights, only the central 5 seconds of each step are considered (5-10 s for zero load, 20-25 s for 0.1 kg, etc.). The selected samples are used to find the best linear fitting based on the least-squares method. The relationship between voltage and force is as follows:

$$F = 11.194\,V - 5.317 \tag{2.1}$$

As showed in Figure 2.9, the linear fitting has a good quality in terms of coefficient of determination (R^2), which means that the load cell has almost a perfect linear behaviour in the range 0-10 N. The equation 2.1 will be used in the acquisition

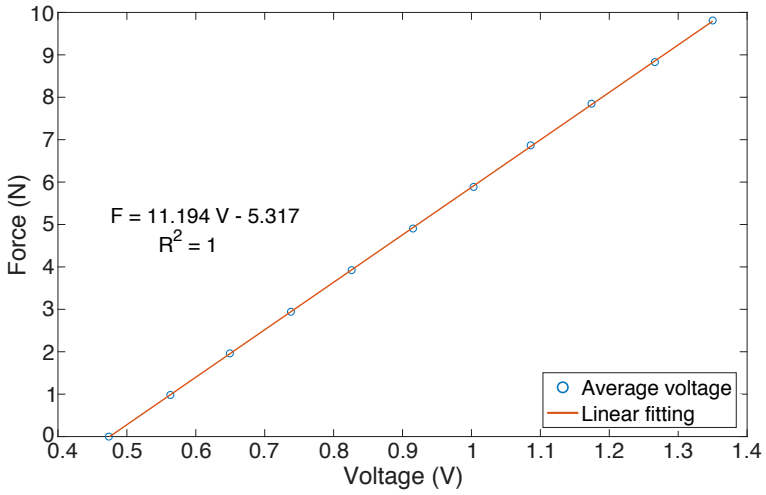

Figure 2.9: Linear relationship between voltage and force. The blue circles are the average voltage values of each step, while the red line is the linear approximation.

system to have directly a force output.

As previously mentioned, another measure of great interest is the angular position of joints. In the proposed instrumented finger, reproducing what Rose did and using the properties of a ring magnet, it is possible to know the relative angular position between two adjacent phalanges. For this purpose, two neodymium magnets diametrically magnetised have been used. These components are placed in correspondence with complementary holes present on the lateral side of proximal and middle phalanges. Since the positioning is achieved by pushing magnets into their allocated space without any additional blocking mechanism, 3D printed parts have to be designed with high precision, so that they can avoid any unintended movement.

Each magnet is coupled with a KMA210, a magnetoresistive angular sensor produced by NXP semiconductors. This device allows to detect changes in the magnetic field, using two orthogonal differential signals deriving from two magnetoresistive sensor bridges. Therefore, when the sensor is placed over a magnet and the relative position between them changes, it perceives a different magnetic field and provides a voltage output which can be connected to a precise angle. These sensors are fixed to the metacarpal and proximal units through an ad hoc 3D printed cover (as shown in Figure 2.10), so as to be placed on top of each magnet.

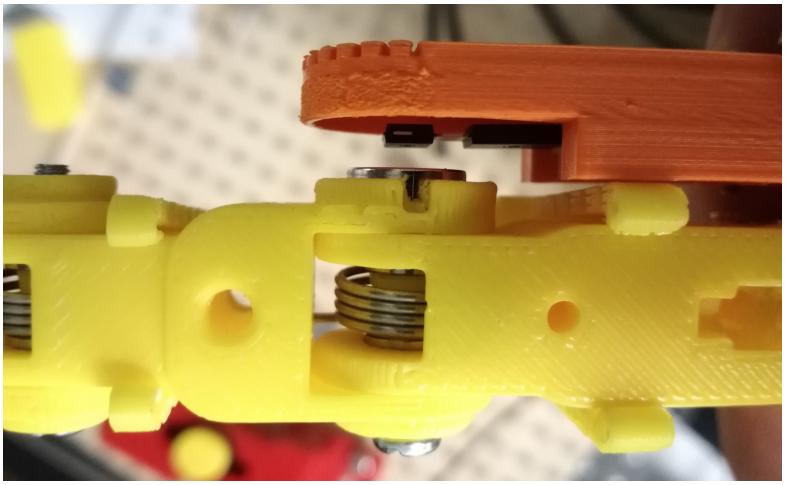

Figure 2.10: Placement of the angular sensor (black item under the orange cover) and its respective neodymium circular magnet. The magnet is pushed into the lateral side of the middle phalanx, while the sensor is inserted in a 3D printed cover, which is then fixed on the proximal unit.

Although KMA210 is a programmable sensor, its preset characteristics (shown in Table 2.2) are fine for the project purpose. However, before using these sensors, a preliminary calibration is necessary. The procedure involves the use of a sheet where a circle is drawn and notable angles are marked, as shown in Figure 2.11. The first operation to do is to place the joint of interest at the centre of the circle. Then, for each marked angle comprised between 0° and 90°, the joint is maintained

Table 2.2: Main characteristics of KMA210 magnetoresistive angular sensor by NXP semiconductors.

Symbol	**Parameters**	**Min**	**Typ**	**Max**	**Unit**
V_{DD}	Supply voltage	4.5	5	5.5	V
$V_{O\ (nom)}$	Nominal output voltage	5		95	$\%V_{DD}$
α_{res}	Angular resolution			0.04	°
$\Delta\Phi_{lin}$	Linearity error	-1		1	°
$\Delta\Phi_{temp}$	Temperature drift error			0.64	°
$\Delta\Phi_{ang}$	Angular error	-1.1		1.1	°

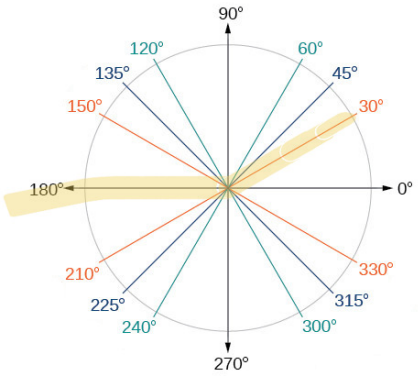

Figure 2.11: Procedure for angular sensors calibration. The joint of interest is placed at the centre of the circle and flexed up to 90°, measuring the voltage value at each angular step.

in position for fifteen seconds and then moved to the next one, while acquiring sensor data at 20 Hz. As the method is susceptible to human error, the acquisition is repeated twice. As can be observed from Figure 2.12, apart from the first step (corresponding to 0°), the acquisitions are comparable.

According to the same principle used for the load cell, only the central five seconds of each step are considered for the calibration. These data are processed via

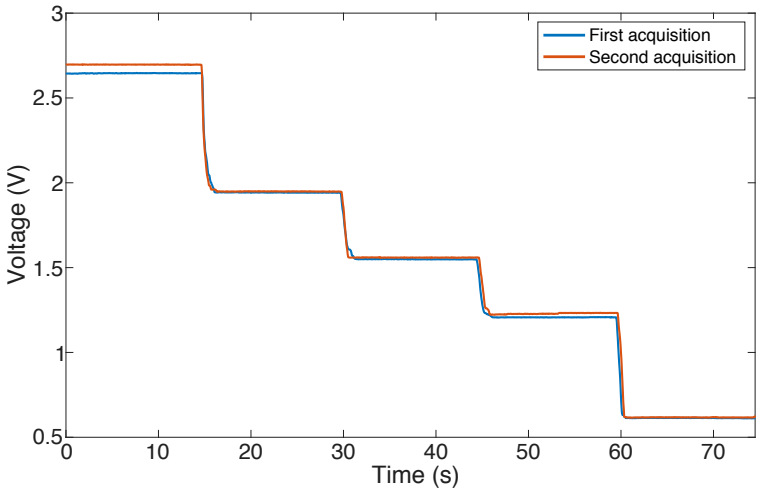

Figure 2.12: Angular sensor output during calibration. Data acquisition is repeated twice.

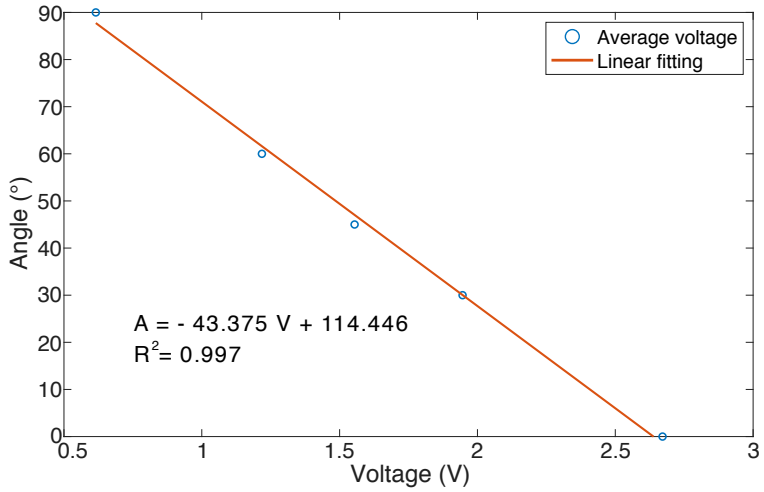

Figure 2.13: Linear relationship between voltage and angle. The blue circles are the average voltage values of each step, while the red line is the linear approximation.

Matlab to find the best linear fitting based on the least-squares method. Despite the rough calibration method, Figure 2.13 shows that also the angular sensor output has a linear behaviour in the range 0°-90°. This statement is confirmed by an R^2 value almost equal to 1 (0.997).

As with the load cell, the linear relationship is included in the motor controller code in order to have directly an angular output.

2.3 Cable routing and motor system

To allow the motor torque to be transmitted to the instrumented finger, the exoskeleton design was implemented based on the design of Kang [18].

Drawing inspiration from this work, a minimal exoskeleton frame has been designed to route flexion/extension cables from the fingertip to the motor pulley. The main objective is to minimize the number of additional components over the finger, while providing the correct amount of torque to move it.

The suggested prototype is constituted of four different units: one fingertip unit, also called thimble, and three straps to direct exo-tendons to the pulley without hindering the finger movement. The thimble has an oval shape (named stadium, to be precise) with multiple grooves both on dorsal and palmar sides, so that

cables can be positioned using slightly different configurations and it is eventually possible to analyse how this affects the exoskeleton operation. Straps are planned to guide the sliding of flexion and extension tendons along the finger: their profile is designed to be compatible with each phalanx and to ensure that they do not suffer any displacement or damage when they are under stress. In particular, the

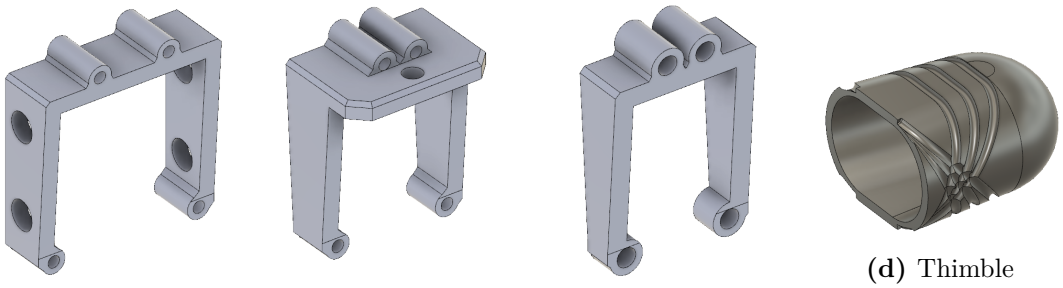

(a) Metacarpal strap **(b)** Proximal strap **(c)** Middle strap **(d)** Thimble

Figure 2.14: Exoskeletons components. Three straps are used along the phalanges, while the thimble is placed on the fingertip unit.

metacarpal segment (Figure 2.14) has two holes on the lateral side, in order to fix it together with the MCP angular sensor, the proximal one is blocked inserting a screw through the phalanx, while the middle one stands stable thanks to the structure of the finger.

All three components exhibit four holes to slide cables: the couple on the dorsal side is intended for extension control, while the couple on the palmar side is for flexion. Before inserting stainless steel wires that mimic the work of human tendons, a Teflon tube is placed as coating to reduce the amount of friction when the cable is pulled/released.

The cable is wound around a 3D-printed pulley, which is in its turn connected to a motor. This component along with the controller has been inherited from Sean Thomas' master thesis project. The system is equipped with a DC motor (RE40, 148867, Maxon), with a gearbox of the reduction ratio of 4.3:1 (GP 42C, 203144, Maxon). Table 2.3 is obtained from Maxon datasheet and shows the main characteristics of the motor. Therefore, the combined use of these two components allows to have a nominal output torque equal to 761 mNm.

The general architecture of the robot has been designed taking inspiration from the HMan robot, which is a device developed by the Human Robotics Group at

Table 2.3: Maxon 148867 motor specifications

Motor characteristic (at nominal voltage)	**Value**	**Unit**
Nominal Voltage	24	V
No load speed	7580	rpm
No load current	137	mA
Nominal speed	6940	rpm
Nominal torque (max. continuous torque)	177	mNm
Nominal current (max. continuous current)	6	A
Stall torque	2420	mNm
Stall current	80.2	A
Max. efficiency	91	%
Torque constant	30.2	mNm/A
Speed constant	317	rpm/V
Speed/torque gradient	3.14	rpm/mNm
Mechanical time constant	4.67	ms

Imperial College London. Figure 2.15, which shows the HMan system architecture and how the robot is controlled, comes directly from the official documentation. Choosing to replicate the same configuration is due to the fact that we wanted to maintain its modular structure.

The main part of the motor controller is the ADS50/5 servoamplifier. It has four different modes of operation: in this case it is set to work in current control.

Figure 2.15: General architecture of HMan robot. The motor is controlled in current and it is connected to a host PC with Ethernet link. **pwm**: PWM motor signals. **q**: encoder values. **I**: motor currents. **F**: output force on handle, in Cartesian coordinates. **X**: Cartesian position of the handle

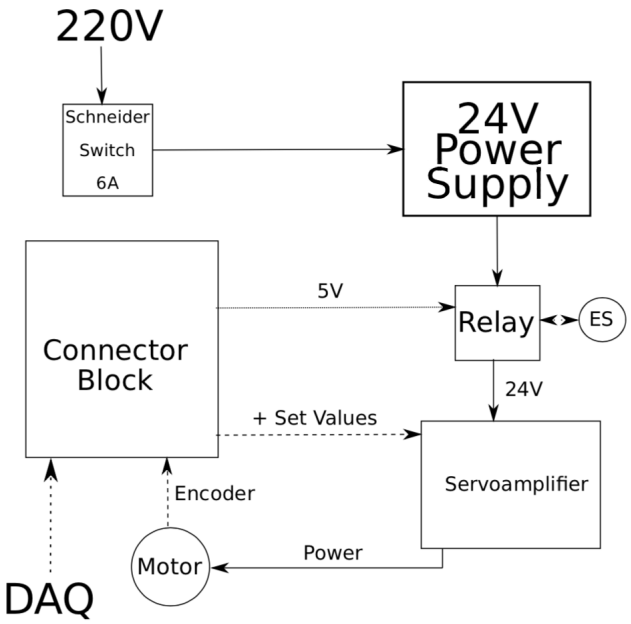

Figure 2.16: General architecture of the motor controller - HMan robot.

As shown in Figure 2.16, the servoamplifier powers and controls the exo-motor by sending defined current values and receives data from a real time PC, which is connected to the controller through a DAQ (PCIe-6343, National Instrument) and its 68-pin connector block. In order to know the position of the motor, an encoder is connected to the NI connector block. Calculations are performed within the target PC and transmitted to the host PC via Ethernet connection.

Motor and load cell wires have been done in a similar way to the ones used for the HMan robot, so as to minimise changes from the original device. The angular sensors are connected to the connector block using the same pin connection.

The functioning of the whole system is managed using a LabVIEW program with multiple subroutines (called subVIs), which handle different small aspects of controlling a motor. Further details of the deployed programs are described in Chapter 3.

Chapter 3

Force prediction model

3.1 Equations of motion for finger joints

The objective of finding a relation between the amount of motor torque and the endpoint force requires a systematic approach to describe joints' motion. In general, the motion of particles and rigid bodies is governed by Newton's law. However, for systems with multiple degrees of freedom, it is possible to undertake a different path, which allows to simplify the derivation of equations of motion.

This method is based on energy conservation and results in a set of equations called Lagrange's equations. For a system of N particles in a conservative force field, their formulation is particularly simple. In fact, considering that each particle has only one degree of freedom, the total kinetic energy using Cartesian coordinates x_i is:

$$T = \sum_{i=1}^{N} \frac{1}{2} m_i \, \dot{x_i}^2 \tag{3.1}$$

For each particle, it is possible to derive the kinetic energy (equation (3.1)) with respect to the appropriate $\dot{x_i}$ and to define the momentum:

$$p_i = \frac{\partial T}{\partial \dot{x_i}} \tag{3.2}$$

By combining the time derivative of the equation (3.2) and the fact that the force can be written as derivative of the potential at the particle position, Newton's

second law can be written as follows:

$$-\frac{\partial V}{\partial x_i} = \frac{d}{dt}\left(\frac{\partial T}{\partial \dot{x}_i}\right) \tag{3.3}$$

As the derivative of V with respect to $\dot{x}_i$ and of T with respect to x_i are zero, equation (3.3) can be rewritten:

$$\frac{d}{dt}\left(\frac{\partial (T-V)}{\partial \dot{x}_i}\right) - \frac{\partial (T-V)}{\partial x_i} = 0 \tag{3.4}$$

Defining the Lagrangian $L = T - V$, the equation (3.4) can be further simplified:

$$\frac{d}{dt}\left(\frac{\partial L}{\partial \dot{x}_i}\right) - \frac{\partial L}{\partial x_i} = 0 \tag{3.5}$$

The equation (3.5) is valid for each particle and allows to describe each degree of freedom just by containing derivatives with respect to x_i and $\dot{x}_i$. A significant advantage of this method is the possibility to use generalized coordinates without modifying the formulation. Moreover, if the system has some non-conservative forces, such as friction phenomena, these can be included on the right-hand side leaving unchanged the rest of the equation.

As mentioned in Chapter 1, in literature there are a few examples for soft exoskeletons where a Lagrangian approach is applied to solve dynamic questions. For the purpose of the project, Lagrange's method is chosen to characterize a multi-DOF system. The instrumented finger's dynamic condition will be separated into two different cases: on-air case, to evaluate the missing parameters of the model (moment arm and friction loss), and contact case, to predict the fingertip force just by adding a new term. Before writing down the equations, it is necessary to consider the developed system, evaluating which assumptions have to be made in order to describe finger motion without over complicating the nature of the equations. Main hypothesis can be summarised as follows:

– The finger is composed by four units: one fixed (metacarpal) and three that can perform flexion/extension movement. Having some preliminary trials while moving the finger, it has been noticed that the DIP displacement can be assumed negligible. For this reason, DIP is considered stationary and

then middle and distal phalanges are regarded as a single rigid body. The Lagrangian model can be used to describe MCP and PIP motions.

– The entire instrumented finger is composed of different materials, including mechanical components (screws, nuts, magnets, etc.). Most of them are uniformly aligned with finger joints and their contribution in terms of inertia can be neglected. Also, their mass has not been taken into account.

– The mass distribution of each phalanx is considered homogeneous and the centre of mass is placed at the mid-length of them. Moreover, phalanges are schematised as lines to simplify the model.

– Only translational and rotational kinetic and potential energy are considered.

– The writing of Lagrange's equations requires to include non-conservative forces on the right-hand side. The proposed model involves two terms:

  1. A friction term, to generally describe losses during joint motion.
  2. A tension-dependent term, which is intended to consider the amount of torque exerted on the joint by the exoskeleton cable.

– As cable tension is not directly measured with dedicated systems, it is derived from motor torque data.

– The instrumented finger is supposed to move only in the sagittal plane, as each joint has one DOF corresponding to flexion/extension.

The assumptions made decrease the number of DOFs to two: this implies that two equations are sufficient to describe the motion of MCP and PIP joints. Figure 3.1 shows the free body diagram of the instrumented finger, which is represented as two yellow lines (one is the proximal phalanx, the other one is the couple composed by middle and distal phalanges). θ_1 and θ_2 are respectively the MCP and the PIP joint angles, measured with angular sensors. Instead, α is the 15° angle designed for the metacarpal unit to mimic wrist extension. The diagram, along with the definition of kinetic and potential energy, helps to define each term of Lagrangian equations.

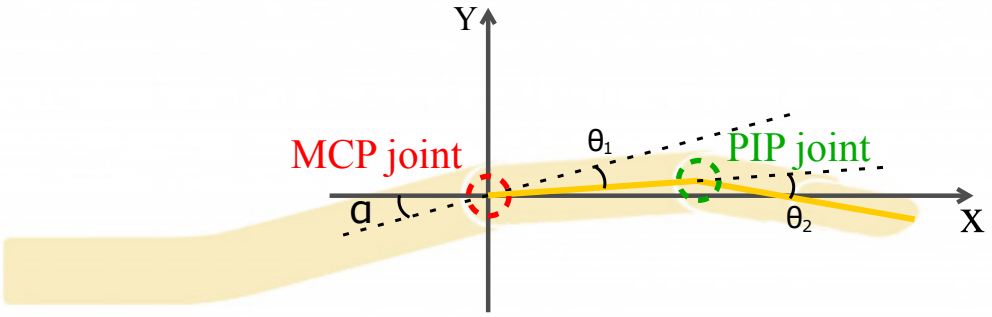

Figure 3.1: Simplified free body diagram of the instrumented finger. Proximal and middle/distal phalanges are schematised as two lines, α is equal to a 15° angle that mimics wrist extension, θ_1 is the MCP angle, θ_2 is the PIP angle. Both of them are positive when the joint is flexed and negative when is extended.

According to the hypothesis listed above, both kinetic and potential energy are composed by two terms: one translational and one rotational. It is equally important to clarify that subscript 1 is associated to the MCP equation (and therefore to the proximal phalanx), while subscript 2 is associated to the PIP equation (and therefore to the single body composed by middle and distal phalanges). The total kinetic energy of the system can be simplified as:

$$T = \frac{1}{2}m_1{v_1}^2 + \frac{1}{2}m_2{v_2}^2 + \frac{1}{2}I_1{\dot{\theta}_1}^2 + \frac{1}{2}I_2{\dot{\theta}_2}^2 \tag{3.6}$$

where the first two terms are the translational kinetic energy and the last two are the rotational kinetic energy. In detail, m_1 and m_2 are the masses of each unit, v_1 and v_2 are the respective translational speeds, $\dot{\theta}_1$ and $\dot{\theta}_2$ are the rotational joint speeds and I_1 and I_2 are the moments of inertia of m_1 and m_2 with respect to the axis of joint rotation.

Similarly, the total potential energy is:

$$V = m_1 g y_1 + m_2 g y_2 + \frac{1}{2}K_{MCP}{\theta_1}^2 + \frac{1}{2}K_{PIP}{\theta_2}^2 \tag{3.7}$$

where K_{MCP} and K_{PIP} are the torsion spring constants (expressed in Nm), g is the gravitational acceleration (approximated to 9.81 m/s^2), y_1 and y_2 are the y-coordinates of each finger unit and θ_1 and θ_2 are the joint angular positions, for MCP and PIP respectively.

Considering that m_1 and m_2 are placed at mid-length of each segment (respectively long $2\,l_1$ and $2\,l_2$), it is possible to express the linear velocity $\vec{v_1}$ and $\vec{v_2}$ in terms of θ_1 and θ_2. Before doing so, it is necessary to evaluate the respective displacements, namely $\vec{r_1}$ and $\vec{r_2}$. The displacement of m_1 is:

$$\vec{r_1} = l_1 \cos(\alpha - \theta_1)\,\hat{i} + l_1 \sin(\alpha - \theta_1)\,\hat{j} \tag{3.8}$$

Time deriving equation (3.8), the velocity of the MCP joint $\vec{v_1}$ is described as follows:

$$\vec{v_1} = \dot{\theta_1} l_1 \sin(\alpha - \theta_1)\,\hat{i} - \dot{\theta_1} l_1 \cos(\alpha - \theta_1)\,\hat{j} \tag{3.9}$$

$$v_1{}^2 = \dot{\theta_1}{}^2 l_1{}^2 \tag{3.10}$$

Analogously, for the PIP joint:

$$\vec{r_2} = 2\vec{r_1} + l_2 \cos(\theta_1 + \theta_2 - \alpha)\,\hat{i} - l_2 \sin(\theta_1 + \theta_2 - \alpha)\,\hat{j} \tag{3.11}$$

$$\vec{v_2} = 2\dot{\vec{v_1}} + (\dot{\theta_1} + \dot{\theta_2}) l_2 [-\sin(\theta_1 + \theta_2 - \alpha)\,\hat{i} - \cos(\theta_1 + \theta_2 - \alpha)\,\hat{j}] \tag{3.12}$$

By simplifying equation (3.12) and applying the sum formula for cosine, it is possible to write:

$$v_2{}^2 = 4 l_1{}^2 \theta_1{}^2 + l_2{}^2 (\dot{\theta_1} + \dot{\theta_2})^2 + 4 l_1 l_2 \dot{\theta_1} (\dot{\theta_1} + \dot{\theta_2}) \cos\theta_2 \tag{3.13}$$

At this stage, kinetic and potential energy (equation (3.6) and (3.7)) can be rewritten in terms of θ_1, θ_2, $\dot{\theta_1}$ and $\dot{\theta_2}$.

$$\begin{aligned} T = & \frac{1}{2} m_1 l_1{}^2 \dot{\theta_1}{}^2 + 2 m_2 l_1{}^2 \dot{\theta_1}{}^2 + \frac{1}{2} m_2 l_2{}^2 (\dot{\theta_1} + \dot{\theta_2})^2 + 2 m_2 l_1 l_2 \dot{\theta_1} (\dot{\theta_1} + \dot{\theta_2}) \cos\theta_2 \\ & + \frac{1}{2} I_1 \dot{\theta_1}{}^2 + \frac{1}{2} I_2 \dot{\theta_2}{}^2 \end{aligned} \tag{3.14}$$

$$\begin{aligned} V = & m_1 g l_1 \sin(\alpha - \theta_1) + 2 m_2 g l_1 \sin(\alpha - \theta_1) - m_2 g l_2 \sin(\theta_1 + \theta_2 - \alpha) \\ & + \frac{1}{2} K_{MCP} \theta_1{}^2 + \frac{1}{2} K_{PIP} \theta_2{}^2 \end{aligned} \tag{3.15}$$

Bearing in mind that the Lagrangian is equal to $T - V$ and the motion can be described by equation (3.5), it is sufficient to derive L with respect to θ_1 and $\dot{\theta}_1$ to define the dynamic motion of the MCP joint. On the right-hand side, friction term ($F_{MCP,loss}$) and torque induced by cable tension (aT) are included:

$$\begin{aligned} &m_1 {l_1}^2 \ddot{\theta}_1 + 4m_2 {l_1}^2 \ddot{\theta}_1 + m_2 {l_2}^2 \ddot{\theta}_1 + m_2 {l_2}^2 \ddot{\theta}_2 + 4m_2 l_1 l_2 \ddot{\theta}_1 \cos\theta_2 + 2m_2 l_1 l_2 \ddot{\theta}_2 \cos\theta_2 \\ &- 4m_2 l_1 l_2 \dot{\theta}_1 \dot{\theta}_2 \sin\theta_2 - 2m_2 l_1 l_2 {\dot{\theta}_2}^2 \sin\theta_2 + I_1 \ddot{\theta}_1 - m_1 g l_1 \cos(\alpha - \theta_1) \\ &- 2m_2 g l_1 \cos(\alpha - \theta_1) - m_2 g l_2 \cos(\theta_1 + \theta_2 - \alpha) + K_{MCP}\theta_1 = aT + F_{MCP,loss} \end{aligned} \tag{3.16}$$

The derivative of L with respect to θ_2 and $\dot{\theta}_2$ gives the PIP equation of motion. In a similar way bT and $F_{PIP,loss}$ are added:

$$\begin{aligned} &m_2 {l_2}^2 \ddot{\theta}_1 + m_2 {l_2}^2 \ddot{\theta}_2 + 2m_2 l_1 l_2 \ddot{\theta}_1 \cos\theta_2 - 2m_2 l_1 l_2 \dot{\theta}_1 \dot{\theta}_2 \sin\theta_2 + I_2 \ddot{\theta}_2 \\ &+ 2m_2 l_1 l_2 \dot{\theta}_1 (\dot{\theta}_1 + \dot{\theta}_2) \sin\theta_2 - m_2 g l_2 \cos(\theta_1 + \theta_2 - \alpha) + K_{PIP}\theta_2 = bT + F_{PIP,loss} \end{aligned} \tag{3.17}$$

Equations (3.16) and (3.17) are intended to describe MCP and PIP joints motion when there is no contact with other objects. To consider cases where the finger is obstructed by obstacles and therefore to evaluate the amount of force exerted by the fingertip, it is necessary to update the PIP equation, considering the amount of torque produced by the contact force. We assume that the force exerted by

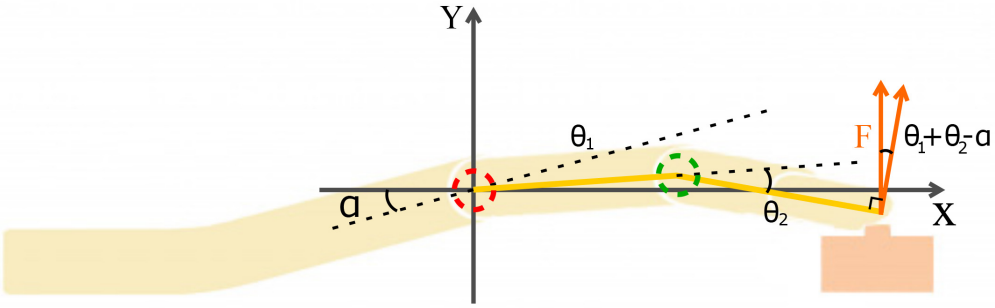

Figure 3.2: Body diagram of the instrumented finger during contact. The force F is perpendicular with respect to the load cell: the component which generates torque on the PIP joint differs by an angle equal to $\theta_1 + \theta_2 - \alpha$.

the fingertip unit is orthogonal with respect to the load cell (which is manually adjusted and validated during experiments). Only the perpendicular component generates a torque on the PIP joint, as shown in figure 3.2, and the force F has to be multiplied by $\cos(\theta_1 + \theta_2 - \alpha)$. The equation (3.17) becomes:

$$\begin{aligned} & m_2 {l_2}^2 \ddot{\theta_1} + m_2 {l_2}^2 \ddot{\theta_2} + 2m_2 l_1 l_2 \ddot{\theta_1} \cos\theta_2 - 2m_2 l_1 l_2 \dot{\theta_1}\dot{\theta_2} \sin\theta_2 + I_2 \ddot{\theta_2} \\ & + 2m_2 l_1 l_2 \dot{\theta_1}(\dot{\theta_1} + \dot{\theta_2}) \sin\theta_2 - m_2 g l_2 \cos(\theta_1 + \theta_2 - \alpha) + K_{PIP}\theta_2 \\ & = bT + F_{PIP,loss} + 2F\cos(\theta_1 + \theta_2 - \alpha) l_2 \end{aligned} \tag{3.18}$$

Equation (3.18) (along with (3.16) and (3.17) for no contact case) aims to describe the finger motion and to study how different exoskeleton designs and the amount of motor torque affect the endpoint force.

The next section will discuss the experiment procedure and explain how this set of equations is used.

3.2 Experiment design

To validate our device and methods, we used motor position command adapted from HMan Robot and Thomas' thesis to perform repeated finger motions.

The entire motor system is controlled using a LabVIEW program, with multiple

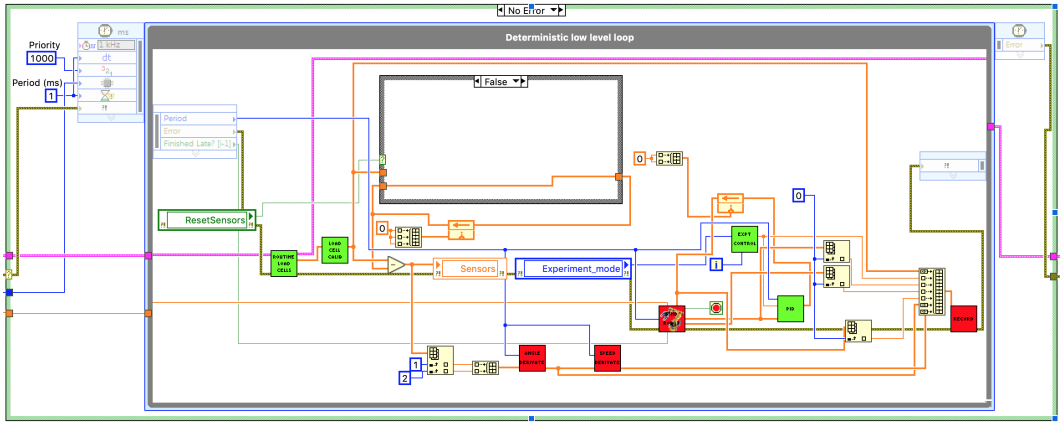

Figure 3.3: Low-level loop of the system. It controls the main functions of the platform.

subroutines (subVIs) dedicated to manage each feature individually.

The main control structure of the robot was rearranged from Thomas' thesis: the low-level loop configuration, shown in Figure 3.3, has undergone only minimal changes, concerning the number of sensors initialised (both angular sensors and the load cell are managed by the DAQ). Other little variations have been introduced in a small group of subVIs, depending on the experiment requirements.

After a series of preliminary trials, in order to select the most suitable operational mode for the project purpose, a sine wave command has been chosen. As a result, the subroutine which manages the type of motor movement has been modified, introducing a sine wave control. The user can modify perturbation amplitude, offset and frequency straight from *Expt_Control* subVI (Figure 3.4).

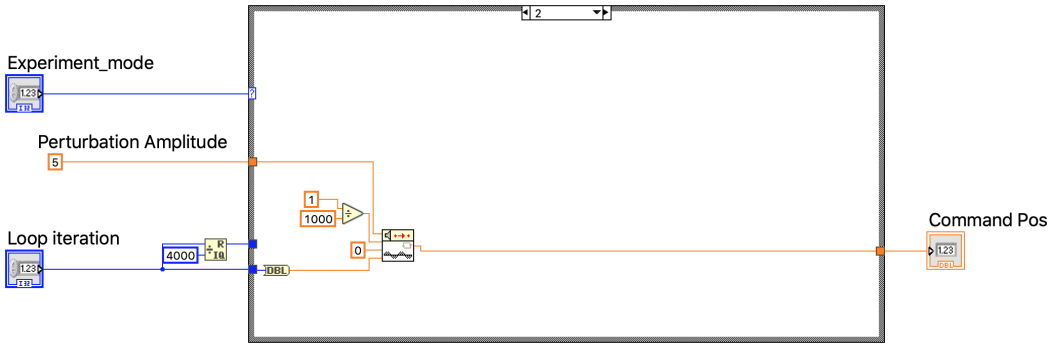

Figure 3.4: Sine wave experiment mode. Perturbation amplitude (expressed in degrees), frequency and offset can be selected by the user.

The experiment protocol is organised in two different phases. During the first phase, also called on-air case (Figure 3.5a), the instrumented finger is controlled with a single cable and repeatedly moved while avoiding the contact with the load cell. MCP, PIP and motor angular position, as well as motor torque, are recorded at 1 Hz frequency and with a 15° motor rotation amplitude. This stage is repeated for ten runs which last 30 seconds each.

Considering that MCP/PIP speed and acceleration can be computationally derived from angular position, it can be noticed that tension moment arms (a and b) and friction losses ($F_{MCP,loss}$ and $F_{PIP,loss}$) are the only terms missing into equations (3.16) and (3.17). Therefore, assuming that these quantities are constant in a defined interval, it is possible to apply a simple linear regression method to

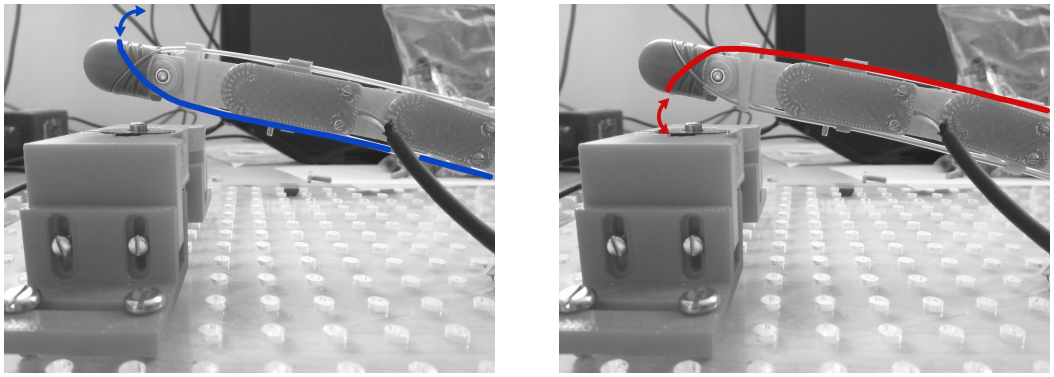

(a) Phase 1 - On-air case **(b)** Phase 2 - Contact force case

Figure 3.5: Experiment phases. During phase 1, the finger is controlled by one extension cable (blue line) and moved freely in the air, without touching the load cell. Phase 2 provides for a cable routing change: the finger is now controlled with one flexion cable (red line) and repeatedly moved to touch the load cell.

evaluate them.

In the second phase, also named contact force case (Figure 3.5b), the cable routing is changed: the extension cable is removed and a flexion cable is wound around the pulley and connected to the finger. Then the finger is cyclically moved, in order to push the load cell with the fingertip unit. No finger movement is visible during this selected perturbation. At this point, the combination of recorded data and estimated parameters allows to predict the exerted endpoint force, by means of equation (3.18).

In both steps, finger motion is controlled through the motor system: in particular, the user has to start the graphical user interface (GUI) of the device, which looks like Figure 3.6 and communicates with the target. Once the main VI is run, the motor is controlled using a series of GUI commands. The *shared enable* button begins the communication between the host PC and the motor controller. At this point, the first action is the motor initialisation: *initialise* button starts a procedure that allows to reset the encoder value (and then the motor position) and the angular sensors to predefined values. The same function, but for the load cell, is deployed by the *reset* button.

When all preliminary operations have been done, it is possible to select the experiment mode by using the arrows of the *shared experiment mode* box. The real

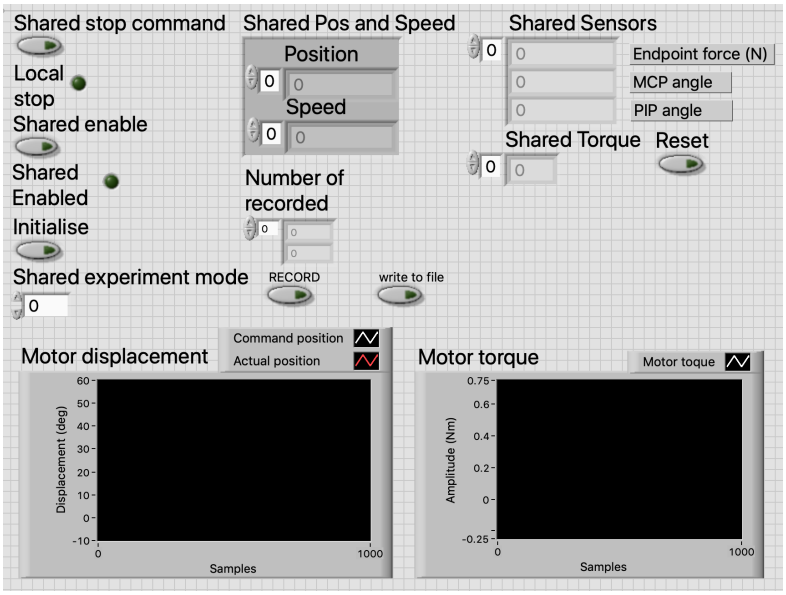

Figure 3.6: Graphical user interface of the motor controller

motor position and its command can be monitored in the lower left corner chart. Motor torque is displayed in real time on the other chart.

To record the data, the *record* button has to be used. The recording can be stopped and started again. *write to file* button allows to save all the acquired data to a text file, where each column contains each time sample of the quantity measured.

Once the acquisition is ended or there is any issue that requires to stop the motor, the *shared stop command* button has to be clicked: the communication between the motor and the controller is interrupted and the local stop light turns red.

Chapter 4

Experiments and data analysis

4.1 4 regions method

As explained in Chapter 3, the experiment protocol is designed in two phases: on-air case and contact force case. The first phase provides for ten on-air runs (30 seconds each), using an exoskeleton configuration with just one extension cable. Data are acquired with a sampling frequency equal to 1 kHz and then processed in Matlab environment.

MCP and PIP angular positions, as well as motor torque, are low-pass filtered using a 4^{th} order Butterworth filter with a cut-off frequency of 5 Hz. This choice is due to the fact that the physiological finger motion has a low frequency band which does not exceed 3-5 Hz (higher frequencies are a sign of pathological states, such as tremor). In addition, a low-pass filter helps to remove any source of high frequency interference or noise. Figure 4.1 shows an example of the filtering process for the MCP joint angle.

The second step of data processing is named regions recognition. Since each term on the left-hand side (LHS) of equations (3.16) and (3.17) is known and tension is derived from motor torque, the only missing terms are the tension moment arms (a and b) and the friction losses ($F_{MCP,loss}$ and $F_{PIP,loss}$). Considering that friction coefficients change depending on whether the finger is in static or dynamic

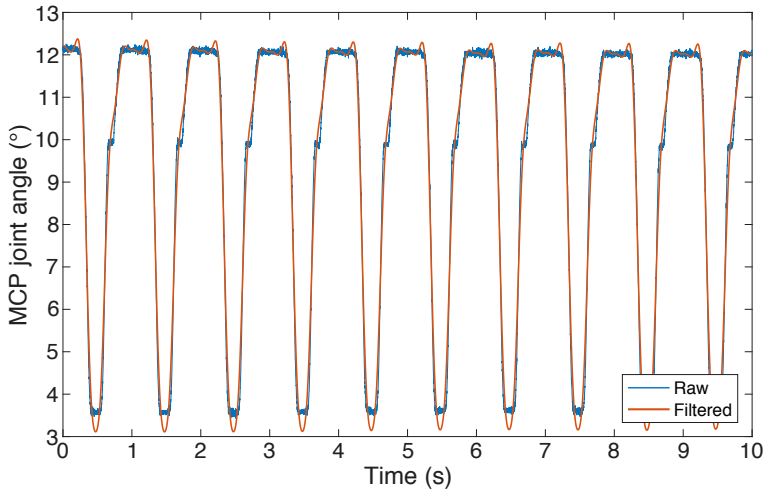

Figure 4.1: MCP joint angle low-pass filtered, using a 4^{th} order Butterworth filter with cut-off frequency of 5 Hz.

conditions, we supposed to identify four different regions during the sinusoidal motion, namely flexion, extension and two static regions in between them. Assuming that missing parameters are constant within these regions, it has been possible to estimate the couple moment arm - friction loss for each region by applying a simple linear regression.

The algorithm to recognize each region of motion is based on joints' speeds and two symmetric thresholds. MCP and PIP speed signals are divided into periods (1 second each) and the average speeds over one period are calculated. Then, each sample of the period is compared with two thresholds, which are selected as percentage of the joint speed range.

In Figure 4.2, the method is applied for one on-air trial, using as threshold value the 10% of the speed range to separate into flexion, extension and static (1 and 2) cases. The choice to use a threshold in percentage terms results from the fact that MCP and PIP joints have different flexion and extension speeds and it would be unfair to select a fixed value which is valid for both of them.

At this point, it is plausible to assume that both moment arms and friction losses are constant in each of the identified regions and hence to apply the linear regression method four times (one for each region) to estimate the missing parameters. The LHS of equations (3.16) and (3.17) is calculated for each time sample and used as

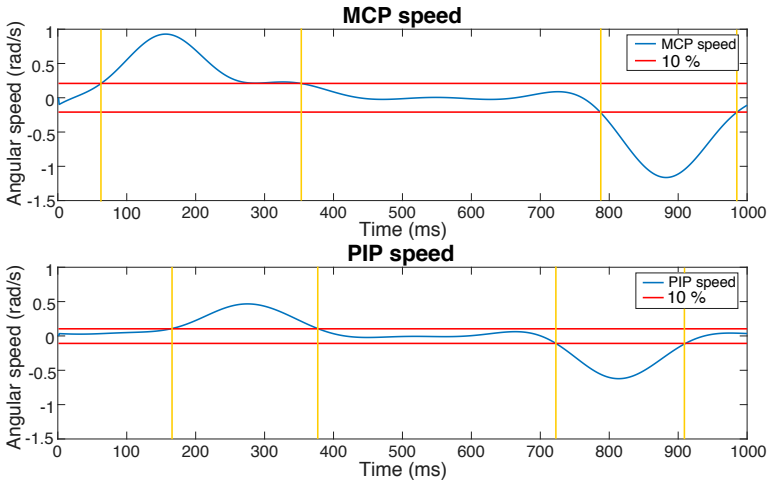

Figure 4.2: Working example of regions recognition algorithm - Four regions. The joints' speed is compared with two symmetric thresholds. The yellow lines define the limits of each region.

an input of *polyfit* function together with the cable tension (independent variable). Values returned from the function are the y-intercept, which corresponds to the friction loss, and the slope of the linear model, which is the moment arm of the cable tension.

The quality of the linear regression is evaluated in terms of R^2, also called coefficient of determination: it measures the fraction of LHS variability that the model is able to explain. Given a series of data observations (y_1, y_2, ..., y_n), their mean value $\bar{y}$ and the correspondent series of fitted data (f_1, f_2, ..., f_n), the coefficient of determination is defined as:

$$R^2 = 1 - \frac{\sum_{i=1}^{n}(y_i - f_i)^2}{\sum_{i=1}^{n}(y_i - \bar{y})^2} \tag{4.1}$$

For an ideal model, each fitted value is equal to the observed value and therefore the numerator of equation (4.1), called residual sum of squares, is zero and R^2 is equal to 1.

For each repetition and region, R^2 values are calculated and shown in Figure 4.3. We can assess that the estimation is acceptable in the flexion region (Figure 4.3b) with a mean R^2 of 0.587, although some runs show low values, and satisfying for

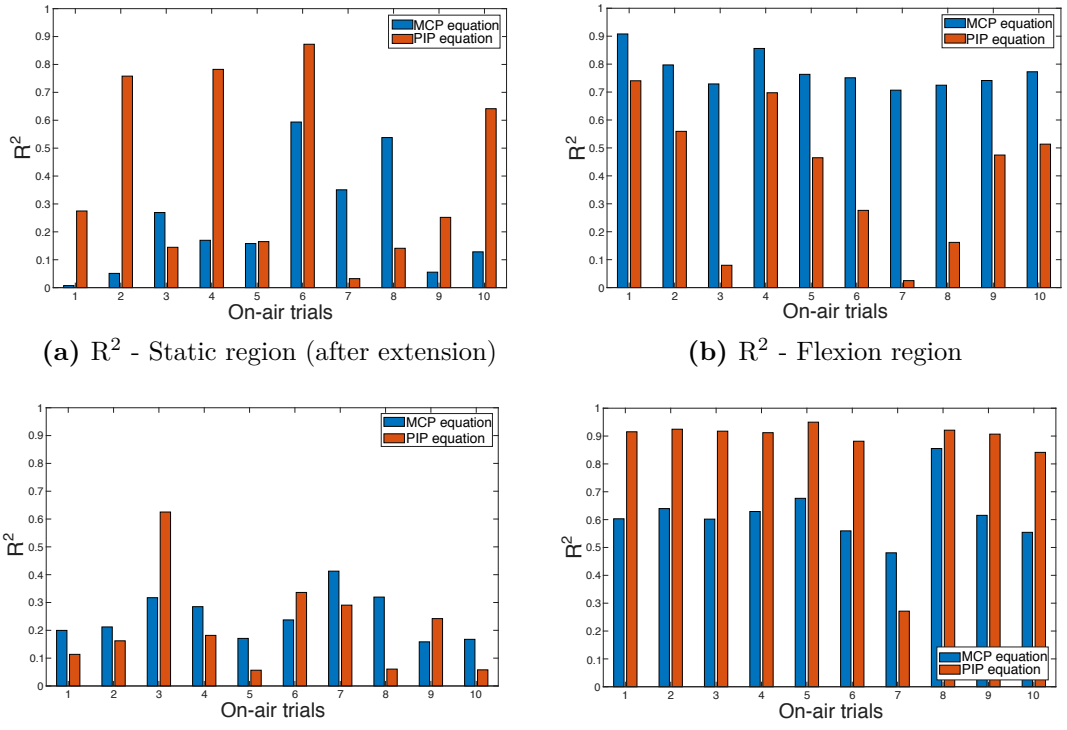

(a) R^2 - Static region (after extension)

(b) R^2 - Flexion region

(c) R^2 - Static region (after flexion)

(d) R^2 - Extension region

Figure 4.3: Parameters estimation accuracy in terms of R^2 - Four regions method. Blue bars indicate R^2 for MCP parameters, while orange bars indicate R^2 for PIP parameters.

the extension region with a mean R^2 of 0.733, in particular for what concerns PIP parameters (mean $R^2 = 0.844$). However, the outcomes in the two static regions are unsatisfactory (mean R^2 of 0.319 and 0.230, respectively).

Before proceeding to the contact force case, all the data which belong to the same region are concatenated, so that it is possible to calculate a single set of parameters for each region and the identified parameters will be used for the force predictive model.

The second phase of the experiment begins with the recording of ten 30-seconds runs, during which the instrumented finger is moved towards the load cell by a single flexion cable. In contrast to the on-air case, the exerted endpoint force is measured.

For each of these trials, the regions recognition method is applied using the same criteria, in order to know the limits of each region. At this point, since all the

equation terms are estimated or known, equation (3.18) for the contact case can be used for evaluating the endpoint force. The developed Matlab code assigns each sample to a defined region and calculates the endpoint force for that time sample by using the correspondent couple of parameters. This process is repeated for the

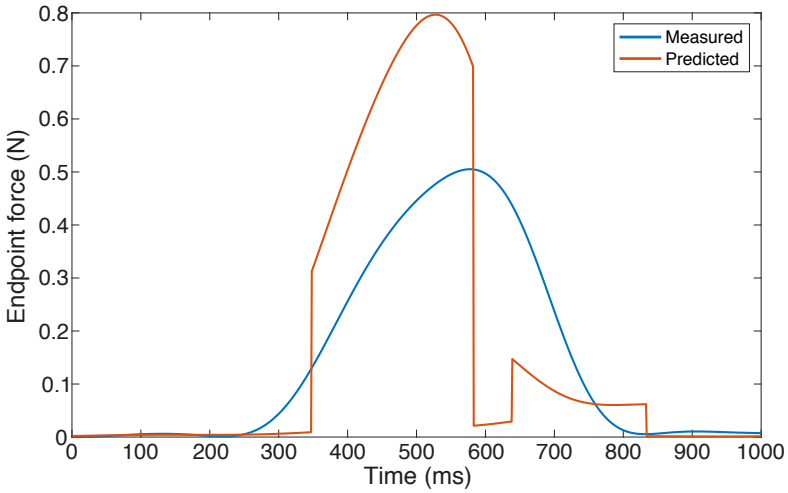

Figure 4.4: Example of force prediction model - Four regions method. When the finger is in one region, parameters are selected accordingly to predict the endpoint force. Model switches from one state to another are particularly evident.

entire duration of the acquisition: Figure 4.4 shows an example recording, so as to highlight how the model works.

By closely analysing Figure 4.4, it is clear that when the finger joint switches from one region to the consecutive, undesired model jumps occur. In particular, the static region in between flexion and extension returns a much lower amplitude with respect to the measured force and alters the shape in a significant way. In general, even though flexion and extension parameters seem to be not good enough for having a reliable force prediction model, the static ones have even lower accuracy and they have to be further examined.

The limits of the four regions method should be sought in the nature of the acquired data. It is necessary to remind that the inputs of the linear regression model are the cable tension, which is directly derived from the motor torque, and the LHS of the equation, which is obtained by acquiring joint position data. Hence, the data distribution on the tension-LHS plane could reveal why the parameters

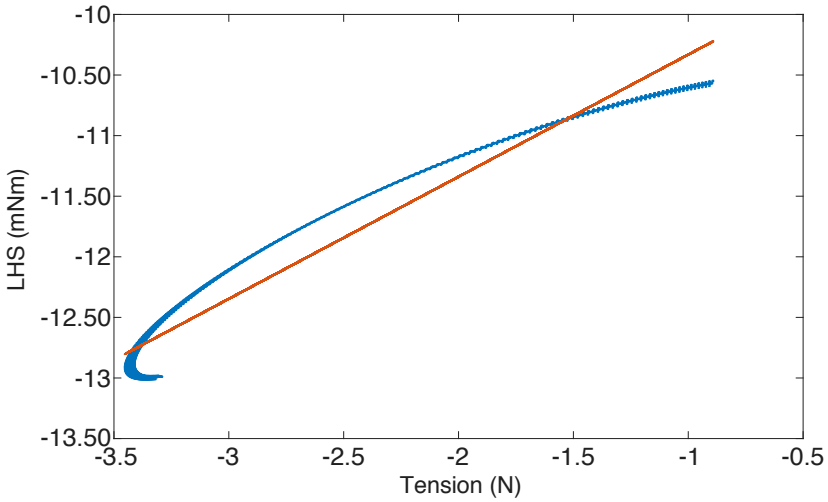

Figure 4.5: Tension-LHS plane - Extension region. Data distribution has a linear trend, except for the tails that can affect the evaluation of the y-intercept.

estimation has a low quality in static regions.

By observing the points distribution on the tension-LHS plane for extension region (Figure 4.5), it can be said that linear regression allows to have a good fitting (average $R^2 = 0.84$), since there is a clear linear trend and only the tails of the distribution affect the estimation of the y-intercept, namely friction loss term.

The situation is completely different in a static region. In fact, as shown in Figure 4.6 for one single repetition, the data distribution is so irregular that some tension values are linked to multiple LHS values and it is unrealistic to get good results just by applying a linear regression approach. It is clear that our simplified system of equations cannot properly estimate the moment arms and the friction losses, but it may be improved by taking into account that some cable elasticity or slack is probably occurring during motion.

Moreover, exploring more deeply the signals acquired during the contact force case, it can be noticed that MCP and PIP speed are almost close to zero and show a reduced speed range (-99.5% for MCP speed, -98.1% for PIP speed with respect to phase one). By applying the same thresholds used for the on-air case, the entire acquisition would require the use of static parameters, as every sample is within thresholds (Figure 4.7). At this moment, it is clear that the presented region recognition has failed to provide accurate estimation and alternatives should be

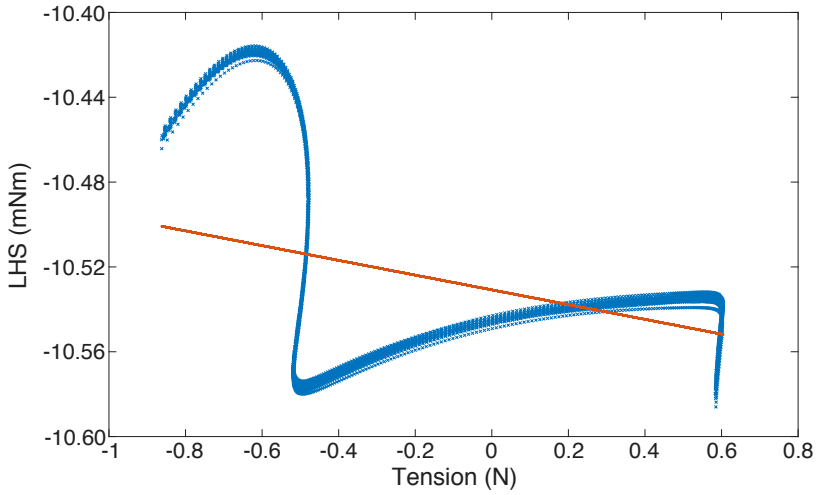

Figure 4.6: Tension-LHS plane - Static region. Data distribution is irregular and some cable tension values are linked to different LHS values.

proposed, considering that static parameters for the PIP equation are the ones with lower accuracy and higher standard deviation (mean R^2 (static 1) = 0.406±0.319, mean R^2 (static 2) = 0.213±0.176).

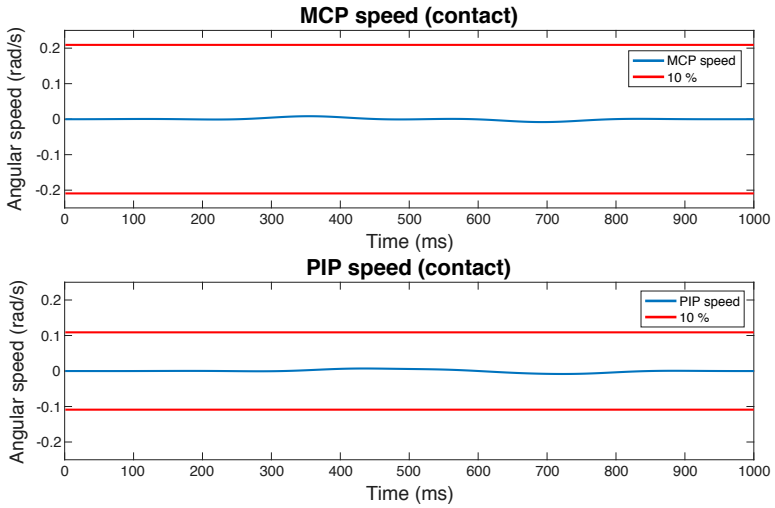

Figure 4.7: Regions recognition algorithm - Contact force case. Using the same thresholds of the on-air case, MCP and PIP speeds are both included between the symmetric thresholds: every sample belongs to the static region.

An alternative solution is to update the region recognition method, by leaving the static regions out and focusing on flexion and extension identification, also evaluating the effect of using different thresholds. To validate the hypothesis, we have tried to predict the endpoint force by using flexion and extension parameters for one entire contact acquisition.

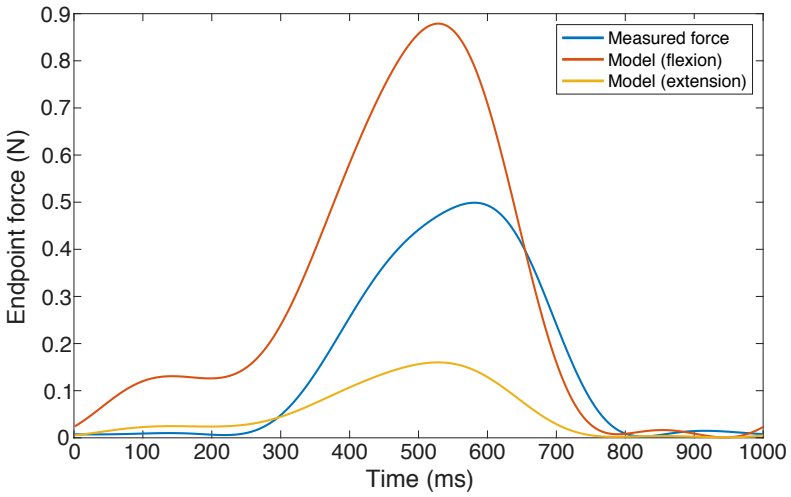

Figure 4.8: Force prediction model using flexion and extension parameters - Four regions method. Regions are not identified in the contact case and one single couple of parameters is applied to predict the fingertip force. In this case, undesired jumps are avoided.

This approach involves one single set of parameters at a time and the results in terms of force shape are promising: the maximum amplitude of the model with extension parameters (yellow line in Figure 4.8) is approximately three times lower with respect to the measured one (0.16 N vs. 0.50 N), while using flexion parameters the maximum reaches 0.88 N. Despite a pronounced amplitude difference between measured and predicted force, the solution that involves using just one set of parameters at a time appears feasible.

Moreover, the new strategy has also drawn attention to the existence of a time delay between measured and predicted force. Hence, the idea is to examine flexion and extension regions in detail (for what concerns the PIP equation), improving the parameters estimation and proposing a method to evaluate and then to compensate the time delay.

4.2 Flexion/extension method

Improving the accuracy of parameters estimation requires an additional analysis on how the linear regression is applied. If LHS and cable tension are normalised (they have different amplitudes) and plotted on a graph considering one period (as we can see in Figure 4.9), it is possible to notice that their shape has a similar trend, but tension is in advance of LHS. The misalignment between the two inputs of the

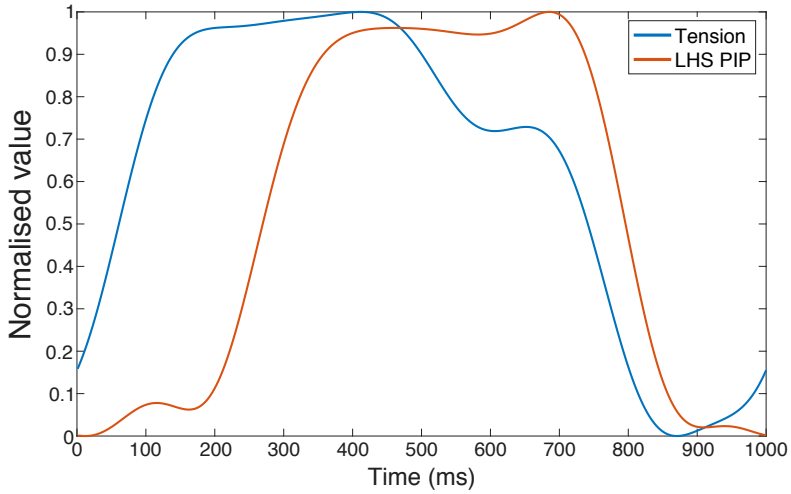

Figure 4.9: Comparison between normalised LHS and cable tension (one period). The cable tension, which is directly derived from the motor torque, has a similar shape but is in advance of LHS.

linear regression could affect the quality of parameters estimation and be the cause of the time delay in the force predictive model. Therefore, the research has been focused on evaluating this delay by improving the alignment between LHS and tension. Once signals are aligned, the regions recognition method is reapplied just for flexion and extension regions and estimation accuracy is evaluated.

The first solution proposed to match LHS with tension is the application of cross-correlation, which is a measure of similarity that allows to evaluate the time delay of one function with respect to another. In this case, the average LHS and tension over one period (1 s) of each on-air trial are normalised and used as inputs for *finddelay*, a built-in function of Matlab which returns the time delay between two input vectors via cross-correlation.

Estimated delays are shown in Figure 4.10: the average delay is 162.2 ms, with a standard deviation equal to 23.2 ms. Each tension signal is shifted by a number

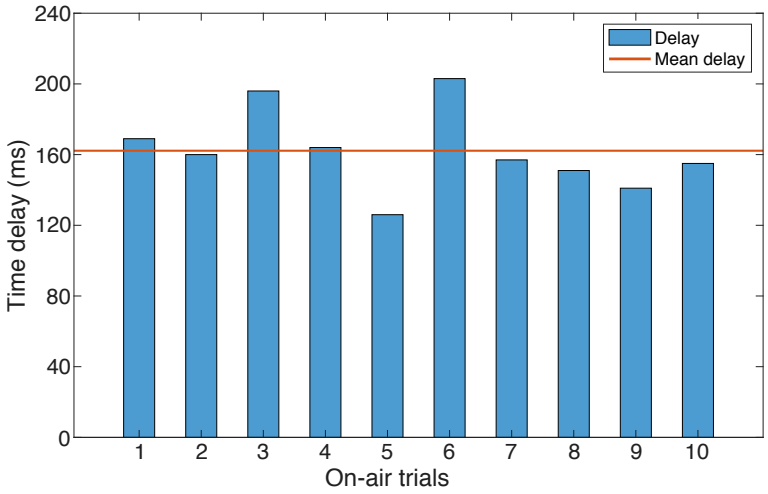

Figure 4.10: On-air trials delay using cross-correlation. The average estimated delay is equal to 162.2 ms.

of samples equal to the time delay and then regions recognition based on flexion and extension is applied to evaluate moment arms and friction losses. Unlike the previous solution, the algorithm recognizes only flexion and extension regions by using two symmetric thresholds, which corresponds to 10% - 20% - 30% of the joint speed range.

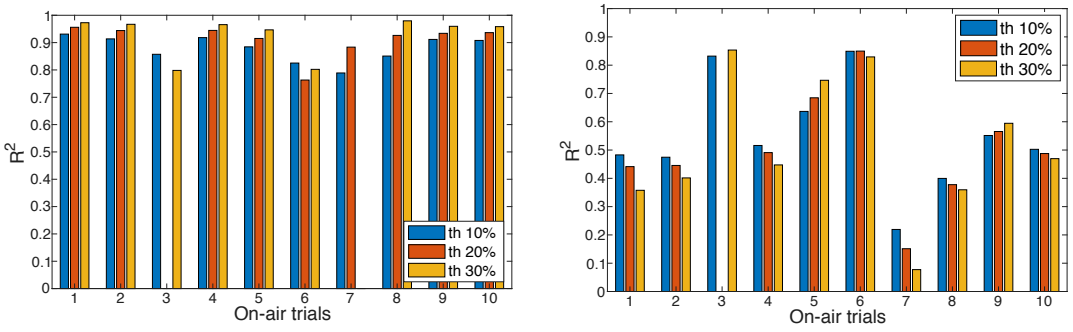

(a) R^2 - Flexion region

(b) R^2 - Extension region

Figure 4.11: Parameters estimation accuracy with time delay (cross-correlation) - Flexion/extension method.

Estimation accuracy is evaluated in terms of R^2, as PIP parameters directly condition the force predictive model. As we can observe from Figure 4.11, the inclusion of a delay term induces opposite outcomes: in flexion region, R^2 improves for all ten trials with respect to the 4 regions method with no delay (Figure 4.3b), while for extension region there is a general worsening of estimation accuracy. In addition, the use of different speed threshold slightly affect the R^2 value. When a bar is missing, it means that for that threshold it has not been possible to select a sufficient number of consecutive samples in flexion/extension regions and then to apply the algorithm for evaluating the parameters.

One possible explanation of these results can be identified by analysing the effect of including a delay term on the LHS-tension alignment. In fact, if we look at the normalised LHS and tension in Figure 4.12, the application of a time delay to the tension signal implies a right shift on the graph (the yellow line show the delayed tension). In doing so, the rising slope of LHS, which is highlighted in dark green and corresponds to the flexion region, is better aligned, while the extension region, in light green, is mismatched with respect to the delayed tension. The disparity may be influenced by the fact that the cable which controls the exoskeleton is pulled only in one direction, namely extension: we can suppose that motion transmission

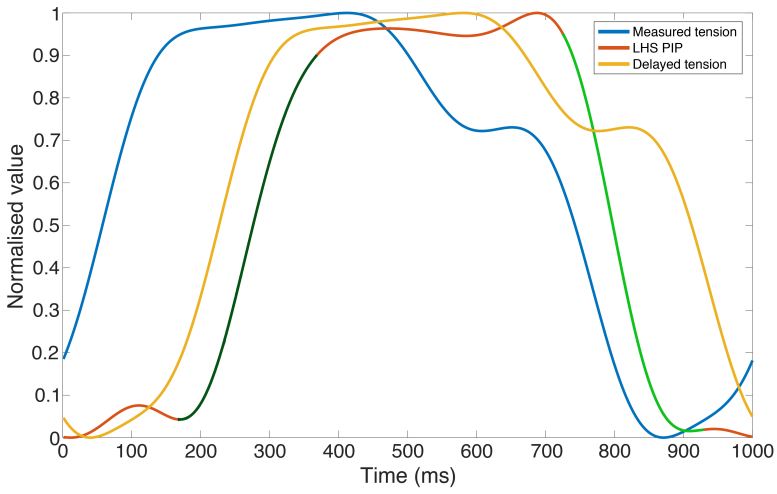

Figure 4.12: Comparison between LHS and cable tension, applying time delay estimated via cross-correlation. The dark green line corresponds to flexion region, while the light green line corresponds to extension region.

is more efficient in such region and therefore a smaller delay occurs.

Assuming that the alignment between LHS and tension influences the parameters estimation, we searched for an alternative method which allows to evaluate the time delay selectively for each region. A suitable solution is offered by the function called *findsignal*, which is another measure of similarity that works minimizing the squared Euclidean distance between signals.

First, it is necessary to identify flexion and extension limits using three different thresholds (10% - 20% - 30%). At this point, according to the time delay you want to evaluate, the average LHS of the above region is selected and compared to the average cable tension over one period. The algorithm identifies the delay in samples (and therefore in ms) which minimizes the squared Euclidean distance. In doing so, it is possible to have an estimation of the delay which is characteristic only of the selected region.

The great advantage of this technique is the possibility to repeat the same procedure also for the flexion region and thus to optimize the alignment of each slope individually.

The effect of the time delay estimation and correction on the extension region is shown in Figure 4.13: LHS, highlighted in light green, is well-aligned with delayed tension.

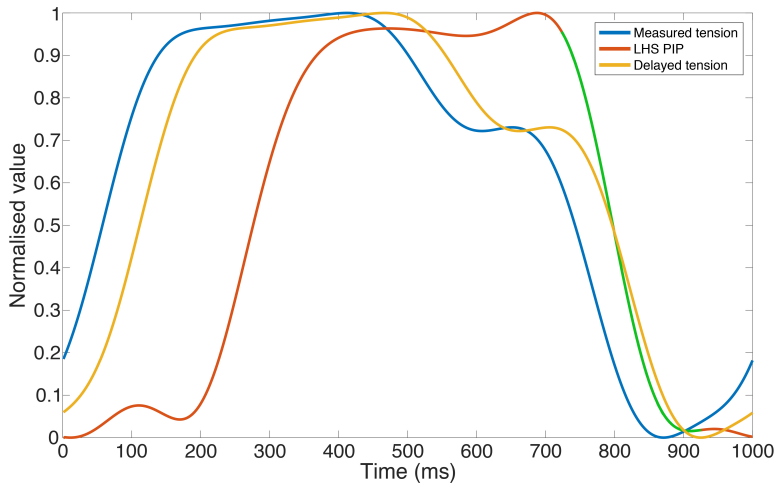

Figure 4.13: Comparison between LHS and cable tension, applying time delay estimated via *findsignal*. The light green line corresponds to the extension region.

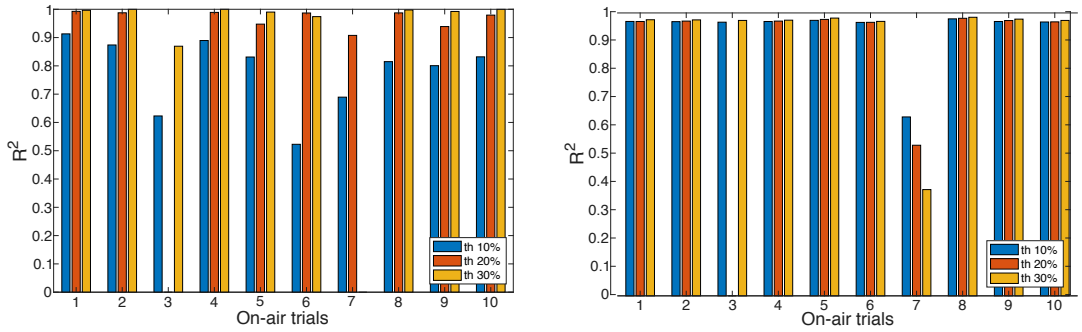

(a) R^2 - Flexion region **(b)** R^2 - Extension region

Figure 4.14: Parameters estimation accuracy with time delay (*findsignal*) - Flexion/extension method.

Once again, it is interesting to evaluate the parameters estimation accuracy, as we did for the cross-correlation case: applying the respective delay, both flexion and extension R^2 assume high values almost for every on-air trials, except number 3 and 7. As for the cross-correlation charts, when the bar is missing in Figure 4.14, it means that was not possible to select a sufficient number of consecutive samples to evaluate the parameters in that region.

Figure 4.15 summarises the average R^2 values for each examined region, method and threshold. It can be noticed that both time delay estimation solutions enhance the goodness of fit in the flexion region (Figure 4.15a). Moreover, considering each method separately, a higher threshold increases the average R^2. For what concerns the extension region (Figure 4.15b), cross-correlation brings down the average R^2

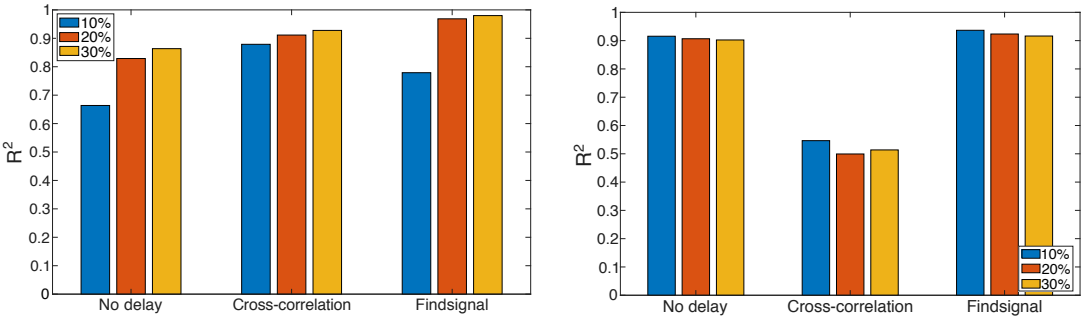

(a) Average R^2 - Flexion region **(b)** Average R^2 - Extension region

Figure 4.15: Estimation accuracy comparison - Average R^2.

value up to around 0.5, while 10% threshold in each technique is slightly preferable to 20% and 30% ones.

In absolute terms, the best set of parameters is the one obtained in the flexion region with *findsignal* and threshold at 30%, with an average R^2 equal to 0.98. However, parameters estimation with a good fit does not mean a good force prediction model necessarily. For this reason, we decided to select the best threshold of each method and to evaluate which are the differences in the second phase of the experiment using these sets of parameters.

The estimated delay can be applied also to contact case trials, so that to compensate the time difference between the amplitude peak of the model and the measured force. However, using flexion parameters, both methods are not effective in solving this issue, rather they worsen the alignment, as you can see from Figure 4.16. Moreover, the amplitude is higher for "no delay" case and much

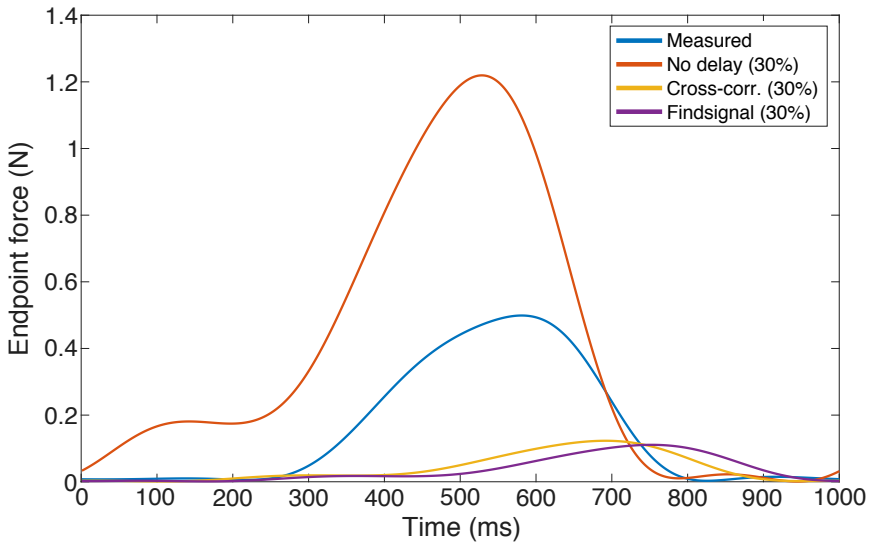

Figure 4.16: Force prediction model using flexion parameters (threshold 30%). Both solutions for time delay estimation are not effective, as they move the amplitude peak of the predicted force beyond the one of the measured force.

lower for cross-correlation and *findsignal* compared to the measured force.

On the contrary, extension parameters, regardless of the chosen method, provide a predicted force which has always a lower amplitude but for *findsignal* technique the delay is compensated (Figure 4.17). In addition, unlike the previous case, the

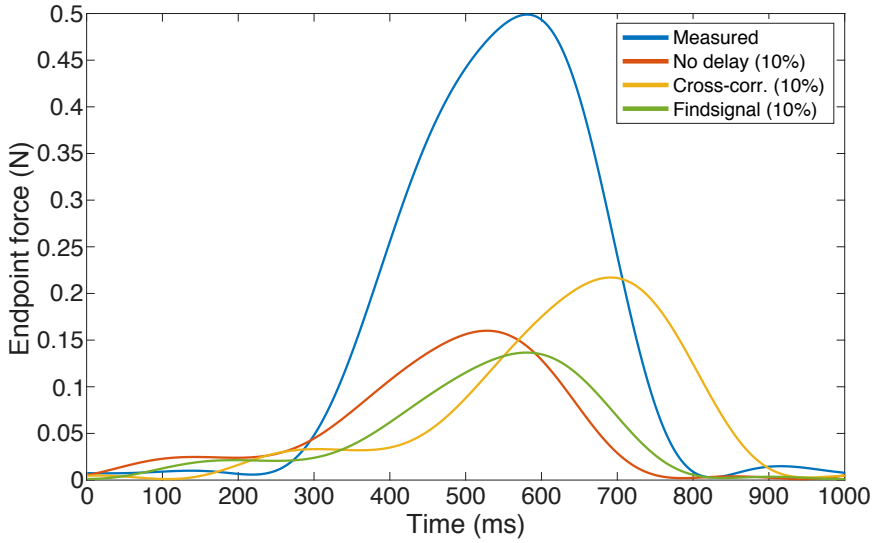

Figure 4.17: Force prediction model using extension parameters (threshold 10%). *findsignal* function for delay estimation allows to compensate the time difference between model and measurement.

use of a different method slightly changes the estimated parameters and then the force amplitude.

By using *findsignal* extension parameters at 10%, the predictive model is applied for each contact trial, in order to evaluate the endpoint force and compare it to the measured one. The tendency is similar to the green line of the example shown in Figure 4.17. To assess the amplitude difference between the model and the measurement, for each repetition the average maximum amplitude of the model and the average difference between maxima have been calculated and summarised in a stacked bar chart (Figure 4.18). As can be seen, the model maximum is a small fraction of the measured force maximum: on average, it corresponds to 27.16%.

Finally, in order to evaluate the goodness of the proposed model in replicating the trend of the contact force, both measured and predicted forces are normalised and compared by calculating the R^2 value. An example trial is shown in Figure 4.19. If the comparison is repeated for every contact repetition, R^2 is equal to 0.97 on average, which tells that the model has the potential to replicate the endpoint force, even though the parameters estimation technique is still problematic to obtain a reliable approach.

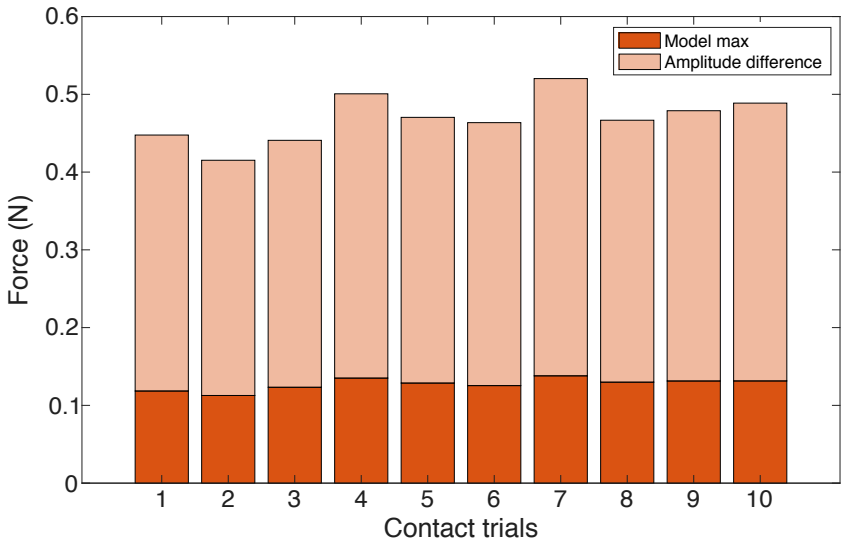

Figure 4.18: Average amplitude difference between measured and predicted force - Contact trials. The maximum amplitude of the model is almost four times lower than the maximum of the measured endpoint force

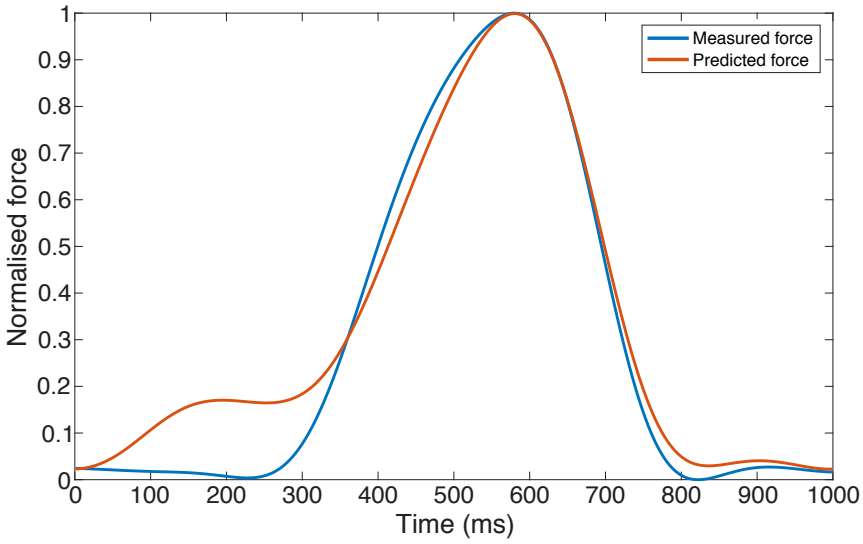

Figure 4.19: Normalised measured and predicted endpoint force - *findsignal* 10%. There is an inconsistency in the first 200 ms, but then the model traces the measured force with high accuracy. The average R^2 value is equal to 0.97.

Chapter 5

Discussion

The developed instrumented platform is intended for providing a low-cost solution to systematically investigate into the control of soft hand exoskeleton, in order to improve their future design. The actual motor controller has been programmed to perturb the 3D-printed finger with a cyclic motion, giving the opportunity to the user to select rotation amplitude, frequency and offset. However, the modularity of the whole system and the structure of the LabVIEW program which manages the motor permit to implement alternative motion commands easily and then to test multiple cable-driven exoskeletons configurations.

The use of a single cable at a time (to flex or to extend the finger, according to the phase of the experiment) has caused some troubles in controlling the instrumented finger: when the pulley moves in the opposite direction to release the cable, the wire is still wound around the drive system, but shows some slack and therefore the finger remains uncontrolled for a small interval of the periodic perturbation. The fact that the motion transmission is somehow interrupted may be the reason for the anomalous behaviour in the static region between flexion and extension. Hence, considering available solutions and trends of soft gloves and hand exoskeletons, the system should be updated by adding a pretension mechanism, in order to avoid cable looseness and consequently unwanted issues during the finger movement.

The four regions method showed considerable limits and therefore may not be suitable for estimating the missing parameters of the Lagrangian model and then for predicting the endpoint force. In fact, the proposed algorithm has shown

unsatisfactory results in terms of R^2 in both static regions (static 1 = 0.406±0.319, static 2 = 0.213±0.176), while barely acceptable for the two dynamic regions.

As for the region recognition algorithm, it must be taken into account that the proposal of using a method based on joints' speeds and two symmetric thresholds arises from the need to identify a limited number of regions in which the missing parameters of the model can be assumed as constant. The initial idea of making a distinction between static and dynamic (flexion and extension) seemed one of the most reasonable, also considering that friction terms undergo clear changes when moving from static to dynamic and vice versa. However, the parameters estimation in static regions has been critical, probably due to the lack of a mechanism which maintains the cable tension during the finger movement.

By using the parameters obtained applying the four regions method, the predictive model shows multiple jumps in correspondence of state transitions. This outcome was partially expected, since each region has its own moment arm-friction loss couple and even a small change among regions cause a discontinuity in the predicted force. Static parameters have revealed themselves much smaller than the ones of flexion and extension and altered the shape of the estimated force significantly.

Updating the region recognition algorithm to flexion and extension regions and using a single set of parameters to predict the endpoint force has led to more promising results. The coefficient of determination assumes higher values in these regions and the force shape looks similar to the measured one, even though the amplitude still shows a considerable difference. For these reasons, we considered the opportunity of including a time delay term in order to improve the quality of parameters estimation and to compensate the delay between predicted and measured force.

The comparison between normalised tension and LHS, which are the inputs of the linear regression, clearly shows a similar shape but a pronounced discrepancy, particularly evident in the rising slope (4.9). Observing the graph, it has been presumed that improving the match between these two signals could have helped in evaluating the delay and achieving a higher quality in parameters estimation. Consequently, two different methods based on a similarity measure have been proposed.

The evaluation via cross-correlation has produced contrary outcomes. R^2 for flexion parameters has increased, stating that data distribution in tension-LHS plane is more linear when the tension is delayed. On the other hand, R^2 for extension parameters, which was already good without additional terms (0.844 ± 0.203), has suffered a sharp decrease, reaching an average value of 0.450 ± 0.242 for a 20% threshold. Moreover, it has been demonstrated that the application of the estimated delay in the predictive model does not compensate for the mismatch between model and measurement, which actually worsens.

These outcomes may be explained by observing that the delay between LHS and tension is different between the rising (flexion) and the falling (extension) slopes: the application of cross-correlation only provides a single delay, which is based on the entire period and cannot consistently improve the estimation in both regions. The apparent minor delay in the extension region might be the result of a more effective cable transmission, since the finger is controlled in extension.

The second solution is still a measure of similarity between two different signals, but unlike the previous one, it is based on the minimisation of the squared Euclidean distance and allows for evaluating a delay which is characteristic of the single region and not of the entire signal. Focusing on each region individually, it is possible to estimate two different delays and improve parameters estimation in both regions, as summarised in Figure 4.15.

However, when these parameters are used in the model to predict the endpoint force, the flexion region delay tends to enhance the distance between model and measurement (as happened applying cross-correlation), while the extension delay realigns these signals, increasing the goodness of fit.

It must be noticed that, despite R^2 values for extension and flexion parameters were high enough to expect a good quality predictive model, the amplitude of the force is almost four times lower than the measured one. In general, the model allows a rough estimation of the contact force, but it can be considered satisfying in terms of shape, since the comparison between normalised measured and predicted force gave back an R^2 value of 0.97 ± 0.01.

Our research highlighted the potential to incorporate the proposed model in an open-loop controller, in which the motor torque that moves the exoskeleton cables is adjusted knowing the relation with the endpoint force. However, several

improvements are required before the implementation: dynamic equations are potentially capable of replicating the force trend and this is encouraging, but the platform has to be updated and alternative perturbation patterns and cable configurations have to be tested.

Precisely with regards to the low force amplitude, one of the factors that could have influenced the outcomes is the change of cable routing between phase one (on-air case) and phase two (contact force case). In fact, during the on-air motion, the finger is controlled with one extension cable placed on the dorsal side and parameters are estimated based on data acquired with this method. Then, parameters are used to predict the endpoint force, but at this stage the cable which controls the exoskeleton is placed on the palmar side. Although the position difference is minimal, it is not possible to assess that parameters do not change when the cable routing is modified. Therefore, moment arms and friction losses, which are valid for the on-air case, may not be acceptable for the contact case and further tests with the same configuration should be conducted.

Another point which has not been taken into account and may affect the force amplitude is the contact angle. Originally, it was assumed to be vertical with respect to the load cell, as shown in Figure 5.1 with an orange arrow. If the angle is

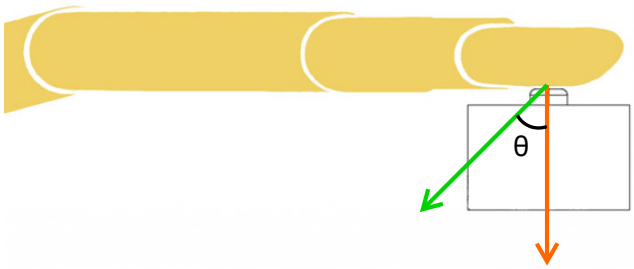

Figure 5.1: Hypothesized finger contact force. The contact force is assumed to be vertical with respect to the load cell: how the model changes if the force has a different direction (identified with an angle θ)?

zero, the model amplitude is significantly lower than the measured one, as already mentioned. However, if we hypothesise to have an angle θ with respect to the vertical line, it is interesting to investigate how the model changes its output.

In order to understand the influence of the contact angle, a single contact trial has been evaluated using five different θ angles: 0°, 15°, 30°, 45°, 60°. The predicted

force over one single period (1 s) is shown in Figure 5.2: increasing the value of θ, the amplitude peak increases, thus moving closer to the data acquired with the load cell. This behaviour also implies a higher R^2 value, which is 0.885 for θ equal to 60°.

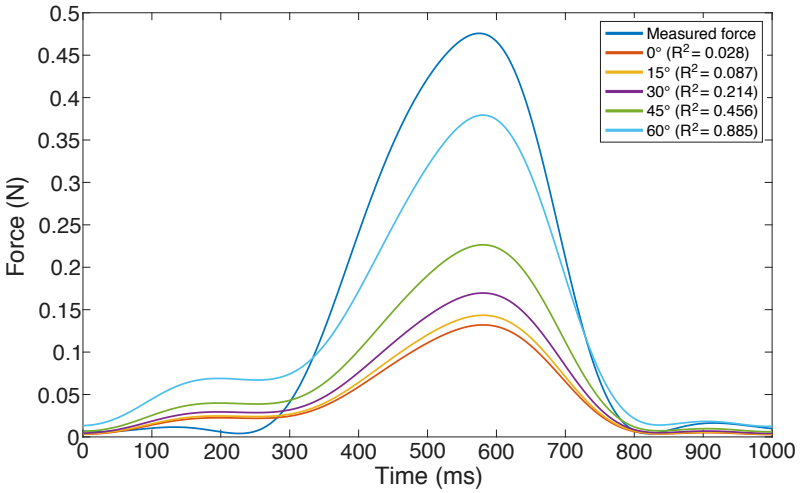

Figure 5.2: Influence of the contact angle on the predicted force. When the angle of contact θ increases, the predicted force amplitude follows the same trend.

In any case, the assumption on the contact angle does not claim to be the only cause which leads to a rough force predictive model, but we wanted to show that can be a factor to take into consideration when additional analysis will be performed.

Finally, it must be considered that the proposed Lagrangian model relies on an indirect measure of the cable tension, which comes from the motor torque. From this point of view, a direct measurement of the cable tension along with a pretension mechanism could help in having a good quality model.

Chapter 6

Conclusion

The developed instrumented platform represents an innovative and affordable solution which allows to perform a systematic investigation in the field of soft hand exoskeleton control. The proposed system is equipped with a 3D-printed finger which has two angular sensors to measure the angular position of the metacarpal and proximal joints. Its motion is controlled by a cable-driven exoskeleton connected to a DC motor, which is programmed to provide a cyclic perturbation. The load cell placed on the platform is supposed to measure the force exerted by the fingertip unit.

In general, it can be said that the device allows to test different configurations and alternative exoskeletons designs made of soft and compliant components. Moreover, by slightly change the code which manages the motor motion, it would be easy to impose other kind of perturbations, which could be relevant in further analysis.

The obtained finger movements were highly reproducible, both for on-air and contact cases, but it has been noticed that the cable is a little loose when it is released by the drive system. The inclusion of a pretension mechanism would improve this issue and consequently could lead to a better performance in terms of parameters estimation, which has been the most critical phase of the experiment.

At the beginning, the use of the Lagrangian approach to simplify the dynamic equations and to predict the fingertip force has led to unsatisfactory results, as the model showed low accuracy and large undesired prediction jumps. By

implementing a delay term, which is based on the minimisation of the squared Euclidean distance, we were able to compensate the time difference between the model and the measurement and also to improve the fit in terms of shape.

Despite the promising improvements, the peak amplitude of the proposed model is still around four times lower than the measured one and the actual solution cannot be incorporated for developing an open-loop controller. In order to do so, it is essential to upgrade the platform, to improve the parameters estimation technique and to plan a thorough investigation into cable configurations.

Bibliography

[1] P. Heo, G. M. Gu, S. Lee, K. Rhee, and J. Kim. «Current Hand Exoskeleton Technologies for Rehabilitation and Assistive Engineering». In: *International Journal of Precision Engineering and Manufacturing* 13.5 (May 2012), pp. 807–824 (cit. on pp. 2, 3).

[2] T. J. Armstrong and D. B. Chaffin. «An investigation of the relationship between displacements of the finger and wrist joints and the extrinsic finger flexor tendons». In: *Journal of Biomechanics* 11.3 (1978), pp. 119–128 (cit. on p. 3).

[3] D. H. Kim, S. Heo, and H. Park. «Biomimetic finger extension mechanism for soft wearable hand rehabilitation devices». In: *2017 International Conference on Rehabilitation Robotics (ICORR)*. 2017, pp. 1326–1330 (cit. on p. 4).

[4] B. Hirt, H. Seyhan, M. Wagner, and M. Zumhasch. *Hand and Wrist Anatomy and Biomechanics. A comprehensive guide*. Stuttgart, Germany: Thieme, 2016 (cit. on p. 4).

[5] G. I. Bain, N. Polites, B. G. Higgs, R. J. Heptinstall, and A. M. McGrath. «The functional range of motion of the finger joints». In: *The Journal of Hand Surgery (European Volume)* 40.4 (2015), pp. 406–411 (cit. on p. 4).

[6] A. Go et al. «Heart disease and stroke statistics – 2014 update: a report from the American Heart Association». In: *Circulation* 129.3 (2014), e28–e292 (cit. on p. 5).

[7] E. Stevens, E. Emmett, Y. Wang, C. McKevitt, and C. Wolfe. *The Burden of Stroke in Europe*. Stroke Alliance for Europe, May 2017 (cit. on p. 5).

[8] R. A. Bos, C. J. W. Haarman, T. Stortelder, K. Nizamis, J. L. Herder, A. H. A. Stienen, and D. H. Plettenburg. «A structured overview of trends and technologies used in dynamic hand orthoses». In: *Journal of NeuroEngineering and Rehabilitation* 13.62 (2016) (cit. on p. 5).

[9] B. L. Shields, J. A. Main, S. W. Peterson, and A. M. Strauss. «An anthropomorphic hand exoskeleton to prevent astronaut hand fatigue during extravehicular activities». In: *IEEE Transactions on Systems, Man, and Cybernetics - Part A: Systems and Humans* 27.5 (1997), pp. 668–673 (cit. on pp. 6, 7).

[10] Andreas Wege and Armin Zimmermann. «Electromyography sensor based control for a hand exoskeleton». In: *2007 IEEE International Conference on Robotics and Biomimetics (ROBIO)* (2007), pp. 1470–1475 (cit. on pp. 6, 7).

[11] A. Chiri, F. Giovacchini, N. Vitiello, E. Cattin, S. Roccella, F. Vecchi, and M. C. Carrozza. «HANDEXOS: Towards an exoskeleton device for the rehabilitation of the hand». In: *2009 IEEE/RSJ International Conference on Intelligent Robots and Systems*. 2009, pp. 1106–1111 (cit. on pp. 6, 7).

[12] Y. Hasegawa, Y. Mikami, K. Watanabe, and Y. Sankai. «Five-fingered assistive hand with mechanical compliance of human finger». In: *2008 IEEE International Conference on Robotics and Automation*. 2008, pp. 718–724 (cit. on pp. 6, 7).

[13] T. Shahid, D. Gouwanda, S. G. Nurzaman, and A. A. Gopalai. «Moving toward Soft Robotics: A Decade Review of the Design of Hand Exoskeletons». In: *Biomimetics* 3.17 (2018) (cit. on p. 7).

[14] M. Nilsson, J. Ingvast, J. Wikander, and H. Holst. «The Soft Extra Muscle system for improving the grasping capability in neurological rehabilitation». In: *2012 IEEE-EMBS Conference on Biomedical Engineering and Sciences, IECBES 2012*. Dec. 2012, pp. 412–417 (cit. on pp. 7, 8).

[15] H. In and K. Cho. «Evaluation of the antagonistic tendon driven system for SNU Exo-Glove». In: *2012 9th International Conference on Ubiquitous Robots and Ambient Intelligence (URAI)*. 2012, pp. 507–509 (cit. on pp. 7, 8).

[16] H. In, K. Cho, K. Kim, and B. Lee. «Jointless structure and under-actuation mechanism for compact hand exoskeleton». In: *2011 IEEE International Conference on Rehabilitation Robotics* (2011), pp. 1–6 (cit. on p. 7).

[17] H. In, B. B. Kang, M. Sin, and K. Cho. «Exo-Glove: A Wearable Robot for the Hand with a Soft Tendon Routing System». In: *IEEE Robotics Automation Magazine* 22.1 (2015), pp. 97–105 (cit. on p. 8).

[18] B. B. Kang, H. Lee, H. In, U. Jeong, J. Chung, and K. Cho. «Development of a polymer-based tendon-driven wearable robotic hand». In: *2016 IEEE International Conference on Robotics and Automation (ICRA)*. 2016, pp. 3750–3755 (cit. on pp. 8, 9, 22).

[19] S. Pu, S. Tsai, and J. Chang. «Design and development of the wearable hand exoskeleton system for rehabilitation of hand impaired patients». In: *2014 IEEE International Conference on Automation Science and Engineering (CASE)*. 2014, pp. 996–1001 (cit. on p. 8).

[20] S. Pu, H. Chang, and J. Chang. «Modeling and development of tension force measurement system for cable-driven hand exoskeleton robot». In: *2015 IEEE International Conference on Advanced Intelligent Mechatronics (AIM)*. 2015, pp. 635–640 (cit. on p. 8).

[21] C. G. Rose and M. K. O'Malley. «A Hybrid Rigid-Soft Hand Exoskeleton to Assist Functional Dexterity». In: *IEEE Robotics and Automation Letters* 4.1 (Jan. 2019), pp. 73–80 (cit. on p. 11).

[22] S. N. Yousaf, V. S. Joshi, J. E. Britt, C. G. Rose, and M. K. O'Malley. «Design and Characterization of a Passive Instrumented Hand». In: Dynamic Systems and Control Conference. Oct. 2019 (cit. on p. 11).

[23] C. Rose. *Open-Source Passive Instrumented Mannequins For Wearable Robots*. `https://mahilab.rice.edu/content/open-source-passive-instrumented-mannequins`. 2018 (cit. on p. 13).

[24] `https://druckwege.de/en/home-en/technology/fused-deposition-modelling-fdm` (cit. on p. 15).